Drug Design, Development and Therapy Dovepress

Open Access Full Text Article ORIGINAL RESEARCH

Zuojin Pill Alleviates Precancerous Lesions of Gastric Cancer by Modulating the MEK/ERK/c-Myc Pathway: An Integrated Approach of Network Pharmacology, Molecular Dynamics Simulation, and Experimental Validation

Lan Liang[1,2,*], Chenming He[3,*], Xue Han[4,*], Jia Liu[5], Liuhong Yang[5], Fengjiao Chang[6], Yami Zhang[7], Jie Lin[5,8]

[1]The First Clinical Medical School, Shaanxi University of Chinese Medicine, Xianyang, People's Republic of China; [2]College of Nursing, Shaanxi Energy Institute, Xianyang, People's Republic of China; [3]LongHua Hospital, Shanghai University of Traditional Chinese Medicine, Shanghai, People's Republic of China; [4]Xijing 986 Hospital Department, Air Force Medical University, Xian, People's Republic of China; [5]School of Basic Medical Sciences, Shaanxi University of Chinese Medicine, Xianyang, People's Republic of China; [6]School of Nursing, Shaanxi University of Chinese Medicine, Xianyang, People's Republic of China; [7]The Fifth Oncology Department, Affiliated Hospital of Shaanxi University of Chinese Medicine, Xianyang, People's Republic of China; [8]Shaanxi Provincial Key Laboratory of TCM Constitution and Disease Prevention, Xianyang, People's Republic of China

*These authors contributed equally to this work

Correspondence: Jie Lin; Yami Zhang, Email linjie0921@sohu.com; zhangyamiysh@163.com

Background: Precancerous lesions of gastric cancer (PLGC) represent critical stages in gastric cancer progression, with a high risk of malignancy. Current treatments, such as Helicobacter pylori eradication, show limited efficacy in reversing precancerous molecular changes. Zuojin Pill (ZJP), a traditional Chinese medicine, has demonstrated potential for treating digestive disorders and may offer a promising approach for PLGC intervention.

Objective: This study aims to investigate the therapeutic effects and mechanisms of ZJP in treating PLGC, focusing on its active components, target pathways, and molecular interactions. By using advanced analytical techniques, we provide a scientific foundation for ZJP's potential application in early gastric cancer intervention.

Methods: Using ultra-high performance liquid chromatography-quadrupole orbitrap high-resolution mass spectrometry (UPLC-Q-Orbitrap HRMS), we identified active components in ZJP. A network pharmacology approach was then applied to construct a "ZJP-compound-target-disease" network. Molecular docking and molecular dynamics simulations were conducted to analyze the stability and interactions of the main active components of ZJP with core protein targets in PLGC. Animal experiments were used to validate significant targets and pathways in vivo.

Results: Tangeritin, Isorhamnetin, Caffeic Acid, Azelaic Acid, and Adenosine were identified as the main active components of ZJP in the treatment of PLGC, with key targets including PIK3R1, MAPK3, SRC, JAK2, STAT3, and PIK3CA. Molecular docking and molecular dynamics simulations further confirmed the relationship between compounds and target proteins. The potential molecular mechanism of ZJP predicted by network pharmacology analysis was confirmed in PLGC rats. ZJP downregulated IL-6, TNF-α, c-myc, p-MEK1 and p-ERK1/2, effectively reversing the progression of PLGC.

Conclusion: ZJP can reverse MNNG-induced PLGC, potentially through inhibition of the MEK/ERK/c-myc pathway and regulation of cellular proliferation and apoptosis.

Keywords: precancerous lesions gastric cancer, Zuojin Pill, network pharmacology, molecular dynamics simulations, ERK

Received: 12 September 2024
Accepted: 21 November 2024
Published: 11 December 2024

© 2024 Liang et al. This work is published and licensed by Dove Medical Press Limited. The full terms of this license are available at https://www.dovepress.com/terms.php and incorporate the Creative Commons Attribution – Non Commercial (unported, v3.0) License (http://creativecommons.org/licenses/by-nc/3.0/). By accessing the work you hereby accept the Terms. Non-commercial uses of the work are permitted without any further permission from Dove Medical Press Limited, provided the work is properly attributed. For permission for commercial use of this work, please see paragraphs 4.2 and 5 of our Terms (https://www.dovepress.com/terms.php).

Graphical Abstract

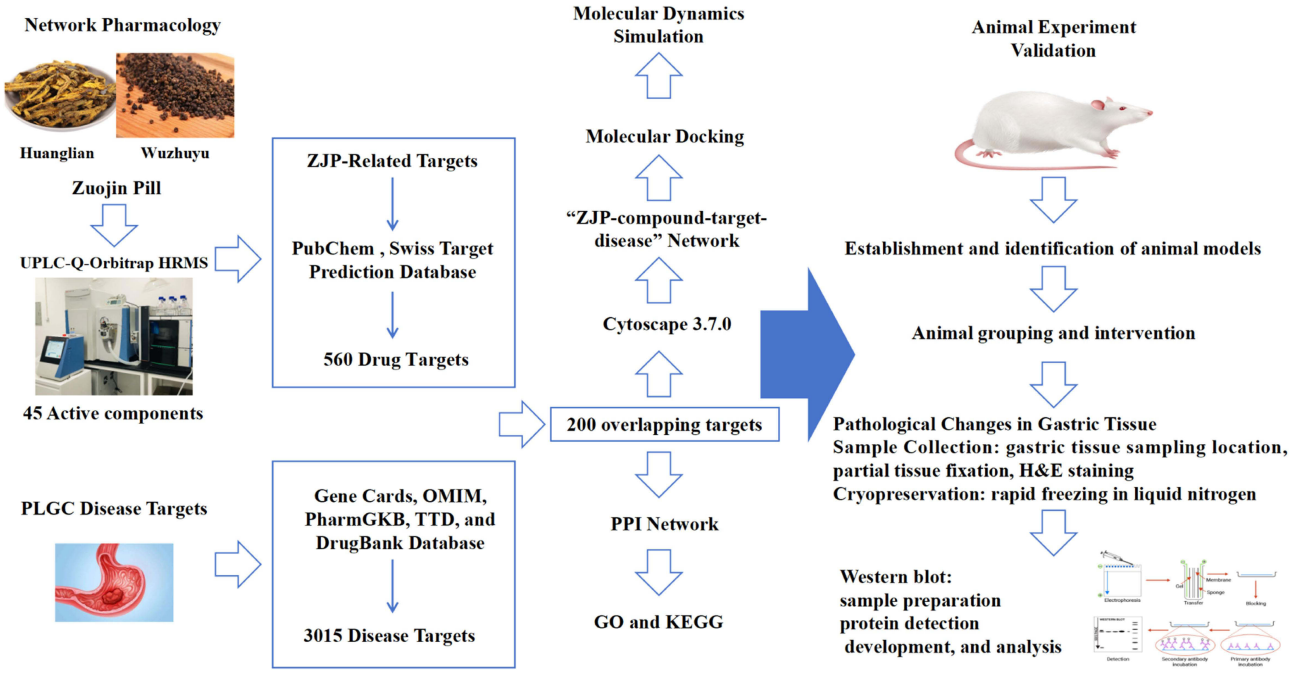

Introduction

Gastric cancer (GC) is the fifth most common malignancy worldwide and the fourth leading cause of cancer-related deaths.[1] Before GC onset, precancerous lesions of gastric cancer (PLGC) often develop in the gastric mucosa, which include chronic atrophic gastritis (CAG), types I, II, and III intestinal metaplasia (IM), and dysplasia (Dys). The progression from CAG to IM to Dys, known as the Correa cascade, is widely recognized as a pathway for intestinal-type non-cardia GC.[2] The incidence of GC at each stage of the Correa cascade is higher than in the general population.[3] A Swedish study estimated that over 20 years, one in 85 patients with non-atrophic gastritis, one in 50 with CAG, one in 39 with IM, and one in 19 with Dys would develop GC, with no gender differences.[4] Although 15–30% of IM may regress after eradication of Helicobacter pylori (Hp),[5] it remains unclear if cancer-inducing molecular changes can be reversed. Long-term observational studies show that the overall incidence of GC does not significantly decrease after Hp eradication, especially if pathological changes have advanced.[6–10] Therefore, PLGC represents a critical link in the "inflammation-cancer transformation" and is a focal point for GC prevention.[11]

The clinical manifestations of PLGC are generally non-specific, including symptoms such as epigastric pain, upper abdominal discomfort, acid reflux, bitter taste, bad breath, and reduced appetite. Notably, symptom severity does not correlate with pathology. Hp infection is a primary cause of PLGC.[12,13] Environmental factors, immunity, genetics, age, and dietary habits also contribute to PLGC risk.[14] Among gastric cancers, Hp infection and other components of the gastric microbiome are significant contributors to GC development.[15] Since the mechanisms underlying PLGC remain unclear, proactive intervention is crucial for GC prevention.

Traditional Chinese Medicine (TCM) has unique advantages in treating digestive diseases due to its molecular complexity and diversity.[16,17] Often used alongside Western treatments, TCM can improve cure and remission rates and inhibit tumor progression.[18] Zuojin Pill (ZJP), a formula created by Yuan Dynasty physician Zhu Danxi, contains *Coptis chinensis* Franch. (Rhizoma Coptidis, HL) and *Tetradium ruticarpum* (Fructus Evodiae, WZY) at a 6:1 ratio. It has been widely documented in clinical practice for treating gastrointestinal symptoms such as stomach pain, nausea, and vomiting.[19–21] Previous studies have confirmed ZJP's anti-inflammatory, anti-acid, and anti-ulcer effects.[22] HL is rich

in alkaloids, notably berberine, which is used to treat cancers, digestive disorders, and metabolic, cardiovascular, and nervous system diseases.[23,24] Berberine also protects intestinal epithelial barriers by inhibiting toxins and bacteria[25] and prevents proliferation and metastasis of various cancer cells.[26] WZY contains evodiamine, an alkaloid beneficial for cardiovascular health and for inhibiting inflammation, fibrosis, and tumor cell apoptosis.[27–31] ZJP exerts anti-inflammatory effects by reducing gastrin-17 and pro-inflammatory factors IL-8, TNF-α, IL-6, and IL-1β, while inhibiting TGF-β1, PI3K, and downstream signaling proteins like p-Akt and p-mTOR.[32] ZJP also targets Hp and protects gastric epithelial cells by modulating pathways such as JMJD2B/COX-2/VEGF and HMGB1/NF-κB.[33] It regulates protein stability and transcriptional activity, inhibiting tumor cell cycle progression, migration, and promoting apoptosis, showing potential in pancreatic, liver, and colorectal cancers.[34–36] However, the effects and mechanisms of ZJP in reversing PLGC remain to be further studied.

This study employs ultra-high-performance liquid chromatography–quadrupole/electrostatic orbitrap high-resolution mass spectrometry (UPLC-Q-Orbitrap HRMS), network pharmacology, molecular docking, and molecular dynamics simulations to explore the active components of ZJP in inhibiting PLGC. Key pathways and targets are validated through in vivo experiments. Initially, UPLC-Q-Orbitrap HRMS identifies ZJP's main active components, and the SwissTargetPrediction database identifies their targets, creating a dataset. Gene Cards, OMIM, PharmGKB, TTD, and DrugBank databases filter PLGC-related targets, which intersect with ZJP's targets to build a "ZJP-compound-target-disease" network and a protein-protein interaction (PPI) network. Topological analysis identifies key active components and targets of ZJP for PLGC treatment. Gene Ontology (GO) and Kyoto Encyclopedia of Genes and Genomes (KEGG) enrichment analyses elucidate the association between ZJP components and signaling pathways. Molecular docking and dynamics simulations confirm the binding stability and interactions between key components and core targets.[37] Finally, an N-methyl-N'-nitro-N-nitrosoguanidine (MNNG)-induced PLGC rat model is used, with Western blotting verifying relevant targets and pathways. This study lays a foundation for further molecular research on ZJP's therapeutic potential in PLGC treatment.

Materials and Methods

Materials and Reagents

Rhizoma Coptidis (Huanglian, HL) (batch number: 1230311) and *Fructus Evodiae* (Wuzhuyu, WZY) (batch number: 20230101) were both purchased from China Shaohuatang National Medicine Co., Ltd. and were certified by experts to meet the 2020 edition of the Chinese Pharmacopoeia. The Ultimate 3000 ultra-high-performance liquid chromatography system and Q-Exactive high-resolution mass spectrometer from Thermo Fisher Scientific, USA, equipped with an electrospray ion source. Micro-ultracentrifuge (D3024R, Beijing Dalong Xingchuang Experimental Instrument Co., Ltd)., pure/ultrapure water system (Direct-Q®5, Merck Millipore, Germany), methanol, and formic acid (Shanghai Aladdin Biochemical Technology Co., Ltd.) were all of chromatographic grade. Ranitidine hydrochloride capsules (batch number H11022491) were purchased from Beijing Cain Technology Co., Ltd., MNNG solution was obtained from Sigma, USA, Vitacoenzyme Tablets (batch number H41024769) were acquired from Luoyang Yilong Pharmaceutical Co., Ltd.; BCA protein assay kit was from Beyotime Institute of Biotechnology, PVDF transfer membrane from Millipore, and ECL DualVue WB Marker from GE Healthcare.

Preparation of High and Low Dose ZJP Solutions

HL (288 g) and WZY (48 g) were decocted twice with water (each time for 1 h, using 10 and 8 times the weight of the herbs respectively as the solvent volume).[38] The decoctions were combined and concentrated to about 336 mL of stock solution by atmospheric evaporation and stored at 4 °C. When used, this concentration served as the high dose (1 g/mL), and was diluted to 0.5 g/mL to serve as the low dose.

UPLC-Q-Orbitrap HRMS Analysis

Preparation of ZJP Sample for Testing

100 μL of high-dose ZJP solution was taken and 400 μL of methanol was added, vortexed for 10 minutes. Centrifuged at 4°C for 10 minutes at 20,000 × g, and the supernatant was collected.

Mass Spectrometry Conditions

A heated electrospray ionization source was used, with alternating positive and negative ion scanning. Ion source spray voltage was 3.2 kV, capillary temperature 300°C, sheath gas flow rate 40 Arb; nebulizer temperature 350°C. Scanning was done using full scan/data-dependent secondary scan (Full MS/dd-MS2) mode, primary resolution 70,000 FWHM, secondary resolution 17,500 FWHM.

Chromatographic Conditions

An AQ-C18 chromatography column (150mm × 2.1mm, 1.8 μm) was used, with a flow rate of 0.3 mL/min and column temperature set at 35°C. The injection volume was 5 μL. The mobile phase consisted of 0.1% formic acid in water (A) and methanol (B). The chromatographic gradient is shown in Table 1.

Network Pharmacology Analysis

Selection of ZJP Active Components

Using UPLC-Q-Orbitrap HRMS, ZJP was separated and identified by injecting the test sample solution and collecting the total ion flow charts in both positive and negative ion modes. Compound Discoverer 3.3 was used for retention time correction, peak identification, and peak extraction. Substances were identified using the Thermo mzCloud online database based on secondary mass spectrometry information. Components with a score of 99 or higher were considered as ZJP active components.

Prediction of ZJP-Related Targets

Active components of ZJP were searched in the PubChem Database (https://pubchem.ncbi.nlm.nih.gov/) to obtain their Compound CID and Canonical SMILES. Using the Swiss Target Prediction Database (http://www.swisstargetprediction.ch/) with "Homo sapiens" and "Probability>0" as filters, effective action targets corresponding to ZJP active components were retrieved. The UniProt (https://www.uniprot.org) protein database was used to standardize gene names of the retrieved targets to establish a dataset.

Prediction and Integration of PLGC Disease Targets

Using keywords "Precancerous lesions of gastric cancer", "Gastric precancerous lesions", and "Chronic atrophic gastritis", disease-related targets were filtered from databases such as Gene Cards, OMIM, PharmGKB, TTD, and DrugBank. After deduplication, potential disease targets were obtained. Using R 4.3.0 (venn package) software, the intersection of the component action targets and PLGC-related targets was plotted in a Venn diagram, representing the action targets of ZJP for treating PLGC.

Table 1 The Elution Gradient

Time (min)	A (%)	B (%)
0	98	2
1	98	2
5	80	20
10	50	50
15	20	80
20	5	95
27	5	95
28	98	2
30	98	2

Construction of the "ZJP-Compound-Target-Disease" and PPI Network

The ZJP action targets and PLGC disease-related targets were imported into Cytoscape 3.7.0 software to construct the "ZJP-compound-target-disease" regulatory network. Co-expressed target information was uploaded to STRING v11.5 (https://cn.string-db.org/), setting the species to "Homo sapiens" and interaction threshold to >0.9 while hiding disconnected nodes in the network to generate a PPI network graph. The file was downloaded in TSV format and imported into Cytoscape to construct the PPI network. Parameters such as degree centrality (DC), betweenness centrality (BC), closeness centrality (CC), eigenvector centrality (EC), local average connectivity-based method (LAC), and network centrality (NC) were used as topology importance parameters to filter out ZJP core components and key targets for visual analysis using Cytoscape.

GO and KEGG Enrichment Analysis

Using the Cluster Profiler package in R4.3.0, GO functional enrichment and KEGG pathway enrichment analyses were conducted. GO functional enrichment included molecular function (MF), biological process (BP), and cellular component (CC). KEGG pathway enrichment analysis elucidated the pathways of ZJP action in inhibiting PLGC. A q-value <0.05 was used as a selection criterion to identify significantly meaningful results for visualization, creating bubble charts and circle diagrams.

Molecular Docking

Key pharmacological substances (small molecules) among the top five by degree value were selected for molecular docking validation with core targets. Core components' 2D structures were downloaded from the PubChem database in SDF format. The 3D structures of core target proteins were downloaded from the PDB database, and small molecule structures (in PDB format) were drawn using ChemDraw 8.0.3 for docking. Water molecules and small molecule ligands were removed using PyMOL 2.2.0 software, and hydrogen was added with AutoDockTools. Molecular docking was conducted between the receptor and ligand, and binding activity was evaluated by docking scores, with the results visualized using PyMOL 2.2.0 and Discovery Studio Client v19.1.0.

Molecular Dynamics Simulation

Molecular dynamics simulation was used to verify the stability and dynamic interactions between proteins and ligands after molecular docking. Proteins and small molecule ligands were separated, and small molecule force field files were generated using the antechamber tool in Ambertools software, then converted into Gromacs force field files using the acpype software tool. Small molecules used the GAFF force field, proteins used the AMBER14SB force field and TIP3P water model. The protein and small molecule ligand files were merged to construct the simulation system for the complex. Molecular dynamics simulations were carried out using Gromacs2022 software under constant temperature, constant pressure, and periodic boundary conditions. During the MD simulation, all interactions involving hydrogen bonds were constrained using the LINCS algorithm, with an integration step of 2 fs. Electrostatic interactions were calculated using the Particle-mesh Ewald method, with a cutoff value set at 1.2 nm. Non-bonded interactions had a cutoff value set at 10 Å, updated every 10 steps. The simulation temperature was controlled at 298 K using the V-rescale temperature coupling method, and pressure was controlled at 1 bar using the Berendsen method. At 298 K, a 100 ps NVT and NPT equilibration simulation was conducted, and the complex system underwent a 100 ns MD simulation, saving a conformation every 10 ps. After the simulation, the simulation trajectory was analyzed using VMD and PyMOL, and the MMPBSA binding free energy analysis between proteins and small molecule ligands was conducted using the g_mmpbsa program.

Animal Experiment Validation

Establishment and Identification of Animal Models

Specific pathogen-free (SPF) male Sprague–Dawley rats (200 ± 20 g) were provided by Chengdu Dashuo Experimental Animals Co., Ltd. (license number: SCXK (Chuan) 2020–030) and housed in a controlled environment with a constant temperature (22 ±2°C), humidity (55%±10%), and a 12-hour light/dark cycle. All studies were conducted in accordance with the Principles of Laboratory Animal Care (Guide for the Care and Use of Laboratory Animals: Eighth Edition. Washington, DC: The National

Academies Press). This study was also approved by the the Ethics Committee of Shaanxi University of Chinese Medicine (Ethics Number: SUCMDL20220602001-1, Supplementary 1). After one week of acclimatization, 50 SD rats were randomly divided using a random number table into a normal group (10 rats) and a model group (40 rats). The normal group was given a standard diet and water, while the model group underwent MNNG compound modeling to establish a PLGC rat model. This involved free access to a light-protected aqueous solution of MNNG (100 μg/mL), alternating gavage every other day with 20% ethanol solution and hot salt water ranitidine (2.25 g/L, 50°C) (2mL/d), combined with irregular feeding patterns (one day fasting, two days feeding) continuously for 28 weeks.[39,40] Rats were randomly selected from the model group at the end of weeks 20, 22, 24, 26, and 28 for euthanasia and immediate abdominal dissection to collect gastric tissues, which were fixed in 4% polyformaldehyde, processed into routine paraffin sections, and stained with HE to observe the degree of gastric mucosa and gland atrophy. Successful modeling was confirmed if intestinal metaplasia occurred in both rats.

Animal Grouping and Intervention

The PLGC model rats were randomly divided into model, Vitacoenzyme, high-dose ZJP (ZJP-H), and low-dose ZJP (ZJP-L) groups, with 8 rats in each group. The ZJP-H and ZJP-L groups were administered (through gavage) oral doses of 1 g kg^{-1} and 0.5 g·kg^{-1} (at a 1:1 ratio), respectively, based on the conversion of body surface area between rats and humans. From week 29, ZJP-H and ZJP-L groups were given the traditional Chinese medicine decoction prepared in Preparation of High and Low Dose ZJP Solutions (2mL/d), and the Vitacoenzyme group received a dosage of 0.30g/kg, all for a continuous 6 weeks. During this period, the model group was given an equal volume of saline by gavage, while the normal group maintained their standard diet and water intake.

Gastric Tissue Pathological Changes

After the last dose, rats were fasted for 24 hours before sample collection. Euthanasia was performed via intraperitoneal injection of 2% pentobarbital sodium (0.225mL/kg), and gastric tissues from the gastric body-antral junction were collected. Part of the tissues were fixed in 4% polyformaldehyde solution, embedded in paraffin, sectioned, and stained with H&E for microscopic observation of morphological changes in the gastric wall. The remaining tissues were snap-frozen in liquid nitrogen and then transferred to a −80°C freezer for storage.

Western Blot

2mL of RIPA lysis buffer containing 100uL of PMSF and 100uL of phosphatase inhibitor was added to EP tubes containing 100mg of gastric tissue along with two steel balls to homogenize the tissue. The homogenate was then centrifuged at 12,000 rpm at 4°C for 15 minutes. The supernatant was transferred to a new 1.5mL EP tube for BCA protein content determination. 50μg protein samples were loaded onto SDS-PAGE gels for electrophoresis and transferred to PVDF membranes. The membranes were blocked with 5% skim milk at room temperature for 2 hours, then incubated overnight at 4°C with primary antibodies against MEK (1:1000), p-MEK (1:1000), ERK (1:1000), p-ERK (1:200), c-myc (1:1000), IL-6 (1:1000), and TNF-α (1:1000). After washing with TBST, membranes were incubated with secondary antibodies (1:5000) at room temperature for 2 hours. Development was carried out according to the ECL chemiluminescence detection kit instructions, and protein expression bands were quantitatively analyzed using Image J software.

Statistical Methods

Data analysis was performed using GraphPad Prism 8.0. Count data that met the normal distribution were expressed as mean±SD. For comparisons between groups, one-way analysis of variance (ANOVA) was used. When variances were homogeneous, pairwise comparisons between groups were conducted using the Least Significant Difference (LSD) method. When variances were not equal, Dunnett's T3 test was used. A p-value of less than 0.05 was considered to indicate statistical significance.

Results

Active Components of ZJP Identified by UPLC-Q-Orbitrap HRMS

Under both positive and negative ion detection modes, total ion chromatograms were obtained as shown in Figure 1 (black for negative ion mode and red for positive ion mode). After screening, 45 active components of ZJP were identified, with their

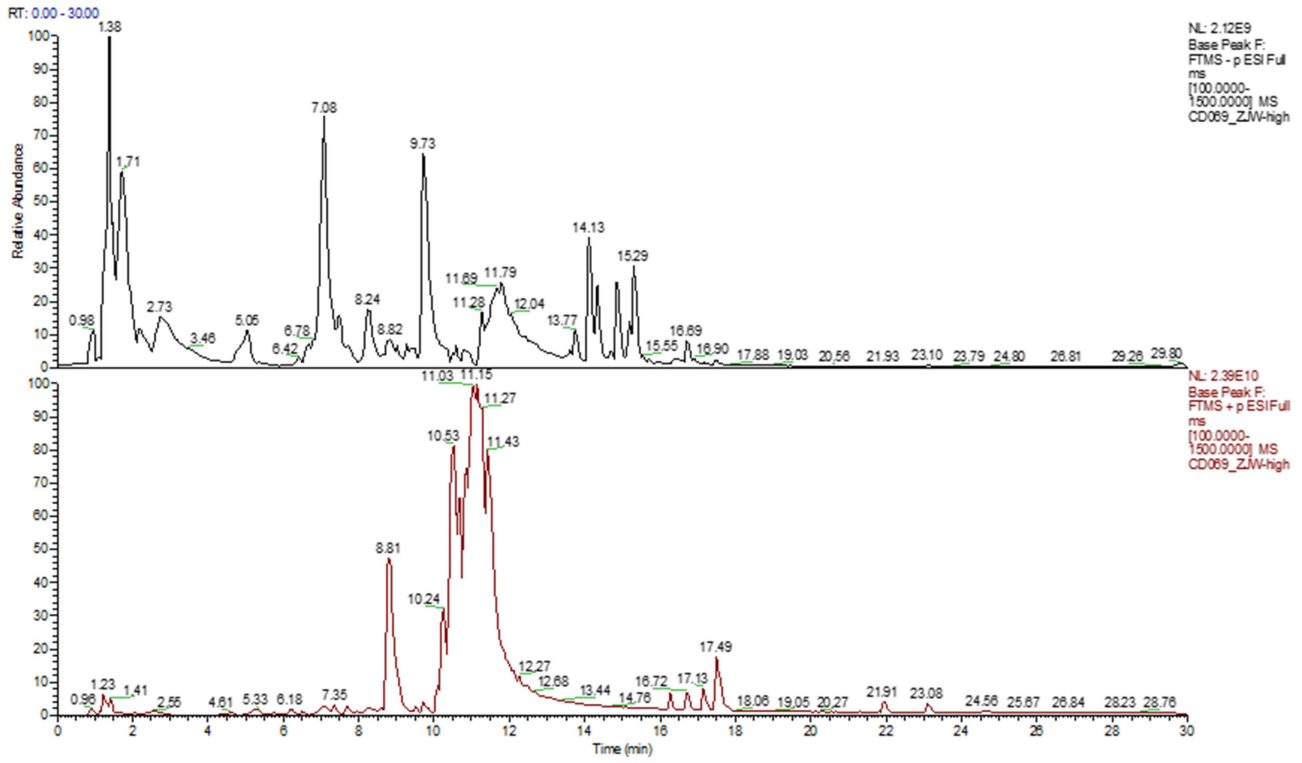

Figure 1 Total ion current spectrum of ZJP in positive and negative ion modes.

CID numbers, active components, peak times, and peak areas listed in Table 2, and further details provided in Supplementary 2.

Network Pharmacology Results

Identification of ZJP Targets for PLGC Treatment

Using the Swiss Target Prediction Database for searching and filtering, and standardizing gene names, 560 targets related to ZJP components were identified. From the DrugBank database, 18 disease targets were identified, from Gene Cards 2582, from OMIM 185, from PharmGKB 312, and from TTD 1 target was identified. After deduplication, a total of 3015 PLGC disease targets were obtained (Figure 2a), and intersecting these with the ZJP-related targets yielded 200 potential action targets (Figure 2b).

"ZJP-Compound-Target-Disease" Network

The "ZJP-compound-target-disease" network was constructed using ZJP active components and PLGC-related targets (Figure 2c). The network includes 243 nodes and 528 edges, where circular green nodes (200) represent action targets, yellow diamond nodes (42) represent active drug components, and a red "V" shaped node (1) represents ZJP. The links between nodes indicate relationships among targets. The network demonstrates that a single active component in ZJP can act on multiple PLGC targets and that multiple active components can share the same target, showcasing ZJP multi-component, multi-target characteristics.

PPI Analysis of Key Targets for ZJP Treatment of PLGC

Two hundred intersecting genes were uploaded to the STRING database, excluding targets with a confidence level below 0.9 and disconnected nodes, to construct a PPI network graph (Figure 2d). Through topological analysis and three rounds of filtering, six core genes were identified (filtering conditions shown in Table 3): PIK3R1, MAPK3, SRC, JAK2, STAT3, and PIK3CA. These genes exhibit strong interactions within the network and are considered potential core targets for ZJP treatment of PLGC (Figure 2e), with their topological parameters listed in Table 4.

Table 2 The Active Ingredients of ZJP

Compound CID	Name	Formula	Calc. MW	m/z	RT [min]	mzCloud Best Match	Reference Ion	Area: CD069_ZJW-high.raw (F434)
60961	Adenosine	C10H13N5O4	267.09672	268.10397	4.619	100	[M+H]+1	4379624074
8988	D-Proline	C5H9NO2	115.06359	116.07087	1.41	99.9	[M+H]+1	4556832075
6925665	L-Phenylalanine	C9H11NO2	165.07898	166.08626	5.318	99.9	[M+H]+1	6059953330
1148	DL-Tryptophan	C11H12N2O2	204.08979	188.0705	7.353	99.9	[M+H-NH3]+1	6859290834
6306	L-Isoleucine	C6H13NO2	131.0947	132.10197	2.561	99.9	[M+H]+1	7208200682
643798	Citraconic acid	C5H6O4	130.02553	129.01825	5.774	99.9	[M-H]-1	616526938.9
3026	Dibutyl phthalate	C16H22O4	278.15186	279.15915	18.534	99.9	[M+H]+1	1527050316
10257	Bufotenin	C12H16N2O	204.12641	205.13368	4.994	99.9	[M+H]+1	1269260347
6089	N,N-Dimethyltryptamine	C12H16N2	188.13133	189.13861	7.111	99.9	[M+H]+1	416382975.4
243	Benzoic acid	C7H6O2	122.03554	121.02827	9.651	99.9	[M-H]-1	117544828.3
45027869	Lariciresinol 4-O-glucoside	C26H34O11	539.23668	540.24396	11.639	99.8	[M+H]+1	6029675 12.7
6088	N-Methyltryptamine	C11H14N2	174.11574	175.12302	7.005	99.8	[M+H]+1	486975727.6
158980	L-Methionine sulfoxide	C5H11NO3S	165.04606	166.05321	1.326	99.8	[M+H]+1	301101986.7
5281654	Isorhamnetin	C16H12O7	316.05812	317.0654	13.75	99.8	[M+H]+1	367496041.7
938	Nicotinic acid	C6H5NO2	123.03234	124.03962	2.068	99.8	[M+H]+1	587922745.9
338	Salicylic acid	C7H6O3	138.03058	137.0233	13.214	99.7	[M-H]-1	509981454.1
13730	2'-Deoxyadenosine	C10H13N5O3	251.10195	252.10922	4.854	99.7	[M+H]+1	183199251.7
89272	Dipropyleneglycol dibenzoate	C20H22O5	342.14654	365.1358	18.181	99.7	[M+Na]+1	577651132.9
10334120	Luotonin A	C18H11N3O	303.10085	286.09756	16.079	99.7	[M+H-H2O]+1	513426613.6
689043	Caffeic acid	C9H8O4	180.04194	163.03891	10.155	99.7	[M+H-H2O]+1	1787564623
9799386	(1S,3R,4R,5R)-1,3,4-trihydroxy-5-{[(2E)-3-(4-hydroxy-3-methoxyphenyl)prop-2-enoyl]oxy}cyclohexane-1-carboxylic acid	C17H20O9	368.11046	369.11774	8.249	99.6	[M+H]+1	374519401.2
68077	Tangeritin	C20H20O7	372.12065	373.12793	17.495	99.6	[M+H]+1	346011944.3

107541	4-Oxoproline	C5H7NO3	129.04141	128.03412	2.709	99.6	[M-H]-1	2952389165
6274	L-Histidine	C6H9N3O2	155.06949	156.07677	1.221	99.6	[M+H]+1	170236557.2
64961	Norharman	C11H8N2	168.0687	169.07597	8.827	99.6	[M+H]+1	358155079.7
1183	Vanillin	C8H8O3	152.04626	151.03899	10.521	99.6	[M-H]-1	114918122
736316	D-Pipecolinic acid	C6H11NO2	129.07918	130.08646	1.728	99.6	[M+H]+1	2053165475
10349	Methylsuccinic acid	C5H8O4	132.04115	131.03387	6.133	99.6	[M-H]-1	269639700.5
3469	Gentisic acid	C7H6O4	108.0201	153.0183	9.378	99.5	[M+FA-H]-1	146226113.7
2776555	2,3-Dihydro-1-benzofuran-2-carboxylic acid	C9H8O3	164.04629	163.03902	11.479	99.5	[M-H]-1	85167182.39
5281643	Hyperoside	C21H20O12	464.09584	463.08878	12.943	99.5	[M-H]-1	974858298.8
6253	Cytarabine	C9H13N3O5	243.08545	244.09268	1.459	99.5	[M+H]+1	185839815.3
333703	4-Indolecarbaldehyde	C9H7NO	145.05162	144.04434	11.827	99.5	[M-H]-1	62019678.55
237332	5-Hydroxymethyl-2-furaldehyde	C6H6O3	126.03197	127.03922	5.957	99.4	[M+H]+1	1679043946
33032	L-Glutamic acid	C5H9NO4	147.05306	148.06033	1.305	99.4	[M+H]+1	1104763165
439227	L(-)-Pipecolinic acid	C6H11NO2	129.07911	130.08638	1.464	99.4	[M+H]+1	3284595518
2266	Azelaic acid	C9H16O4	188.10427	187.09691	13.383	99.3	[M-H]-1	282025853.3
135398634	Guanine	C5H5N5O	134.02292	152.05675	5.376	99.3	[M+NH4]+1	1667295486
7059	6-Methylquinoline	C10H9N	143.07352	144.0808	8.614	99.3	[M+H]+1	2478819120
5570	Trigonelline	C7H7NO2	154.07421	138.05493	1.46	99.3	[M+H-NH3]+1	5427913459
439165	Glucose 1-phosphate	C6H13O9P	278.04022	261.03693	1.637	99.3	[M+H-H2O]+1	4805677 14.8
10177048	(3R,5R)-1,3,5-Trihydroxy-4-{[(2E)-3-(4-hydroxy-3-methoxyphenyl)-2-propenoyl]oxy}cyclohexanecarboxylic acid	C17H20O9	350.10054	349.09326	12.109	99.2	[M-H]-1	100427490.6
1001	Phenethylamine	C8H11N	104.06301	122.09679	4.893	99.2	[M+NH4]+1	189669916
6760	4,7,8-trimethoxyfuro[2,3-b]quinoline	C14H13NO4	259.08452	260.0918	15.068	99.2	[M+H]+1	230583133.3
6508	D-(-)-Quinic acid	C7H12O6	192.06341	193.07074	1.639	99.2	[M+H]+1	1316411596

https://doi.org/10.2147/DDDT.S487371

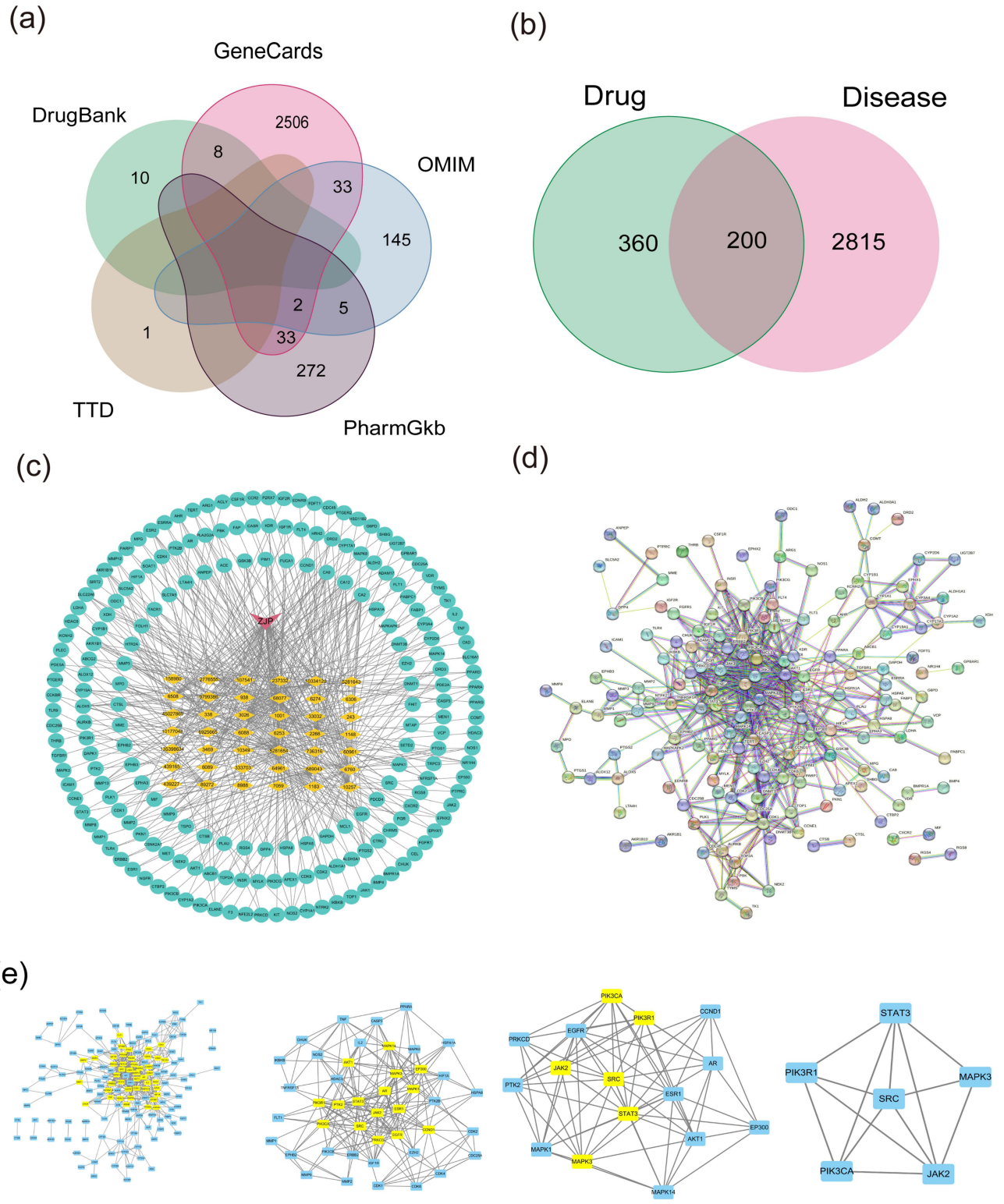

Figure 2 Network pharmacology target analysis. (**a**) Venn diagram of PLGC targets; (**b**) Venn diagram of active ingredient targets of ZJP and PLGC targets; (**c**) Active ingredient-target network of ZJP treatment in PLGC; (**d**) PPI network of targets of ZJP treatment in PLGC; (**e**) PPI network of targets of ZJP treatment in PLGC.

GO and KEGG Enrichment Analysis

Using the R 4.3.0 software with the clusterProfiler package, GO functional enrichment analysis was performed on the 200 common targets, resulting in 3012 entries ($q<0.05$), including 2666 for biological processes (BP), 113 for cellular

Table 3 Filter Conditions of CytoNCA

	Filter 1	Filter 2	Filter 3
BC	35.33	13.497	4.069
CC	0.067	0.521	0.732
DC	4	8.5	9.5
EC	0.019	0.109	0.247
LAC	1.367	4.25	6
NC	2	5.144	7.336

Table 4 Information of Topology Parameters of Core Targets

	PIK3R1	MAPK3	SRC	JAK2	STAT3	PIK3CA
BC	4.382	5.16	13.72	5.176	21.887	4.382
CC	0.75	0.75	0.938	0.75	1	0.75
DC	10	10	14	10	15	10
EC	0.263	0.259	0.342	0.257	0.355	0.263
LAC	6.4	6.2	8	6.4	8.133	6.4
NC	7.631	7.595	13.307	7.928	15	7.631

components (CC), and 233 for molecular functions (MF). The top 10 enriched categories were visualized in bubble charts and circle diagrams. KEGG pathway enrichment analysis yielded 175 entries ($q<0.05$), from which the top 30 enriched pathways were selected for bubble chart visualization (Figure 3a and b). Pathway diagrams were created for the PI3K-Akt signaling pathway, the MAPK signaling pathway, and gastric cancer-related pathways, with red nodes indicating genes at the intersection of ZJP and PLGC (Figure 3c-e).

Molecular Docking Results

Generally, a docking score less than −4.25 k/mol indicates some binding activity, less than −5.0 k/mol indicates good binding activity, and less than −7.0 k/mol indicates very strong binding activity. The docking binding energies are displayed in Figure 3f. For instance, the binding energy between Tangeritin and MAPK3 protein is −8.7 k/mol, indicating strong binding activity. Isorhamnetin shows binding energies of −9.4 k/mol with MAPK3 and −8.7 k/mol with SRC protein, indicating strong binding activity with both proteins. Adenosine has a binding energy of −8.6 k/mol with PIK3CA protein, also showing strong binding activity. These results suggest that these active drug components can stably bind to core target molecules. The docking results visualized using PyMOL 2.2.0 software are shown in Figure 4. From the figure, it can be seen that Tangeritin forms hydrogen bonds with MAPK3 at SER-225, LYS-224, GLY-374, ARG-370, and PRO-373. Isorhamnetin forms hydrogen bonds with MAPK3 at ARG-116, ASP-117, ARG-108, ASP-37, ASP-105, and GLY-39; and with SRC at PHE-307, GLU-310, and GLY-406. Adenosine forms hydrogen bonds with PIK3CA at GLU-259, ASP-258, ARG-662, VAL-166, and GLN-661.

Molecular Dynamics Simulation Results

Based on the results of molecular docking, the MAPK3-Isorhamnetin complex was selected for molecular dynamics simulation.

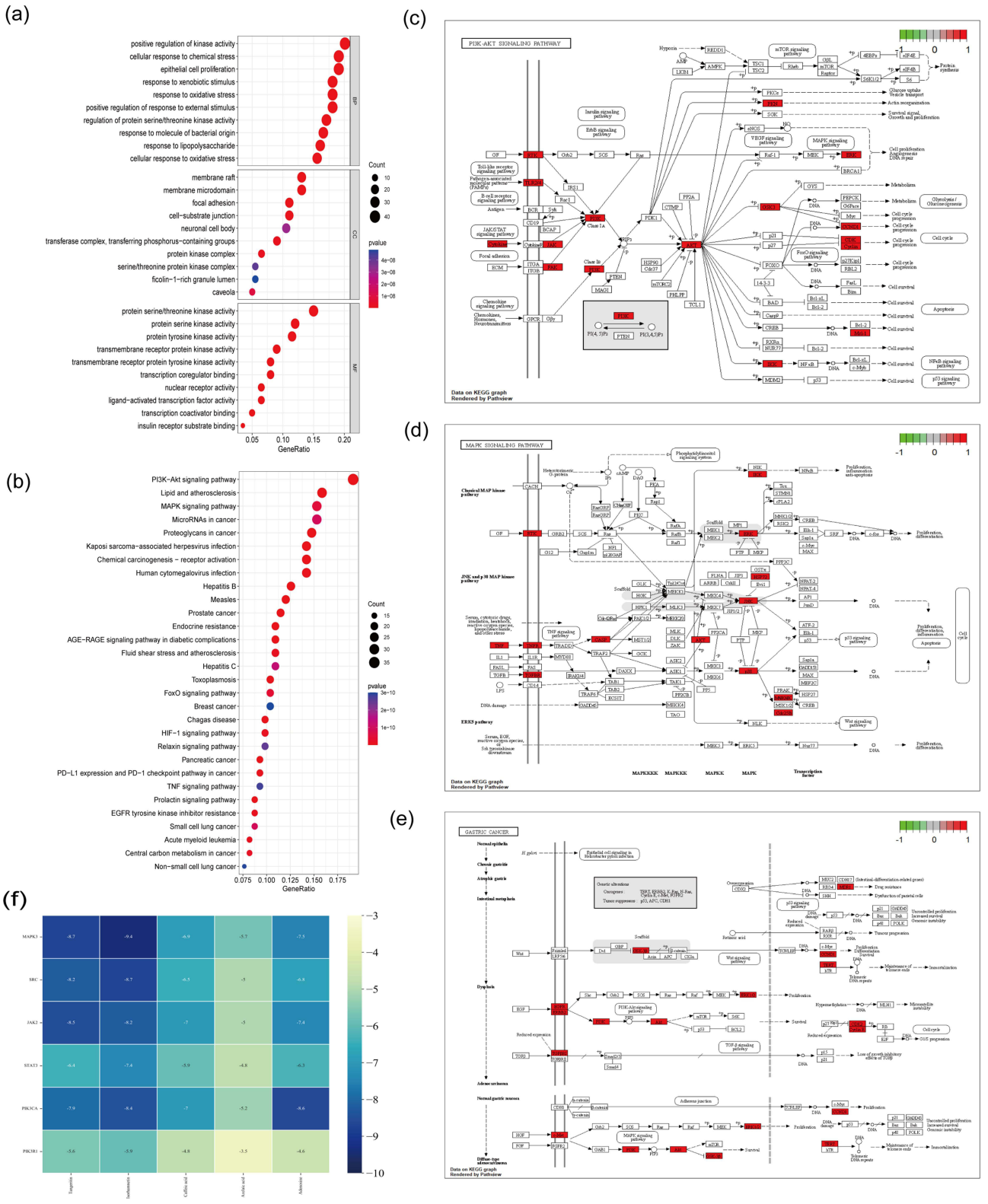

Figure 3 Enrichment analysis of network pharmacological targets and docking binding affinities. (**a**) GO enrichment analysis of core targets; (**b**) KEGG pathway enrichment analysis of core targets; (**c**) PI3K-Akt signaling pathway; (**d**) MAPK signaling pathway; (**e**) GASTRIC CANCER signaling pathway; (**f**) The results of the docking binding affinities.

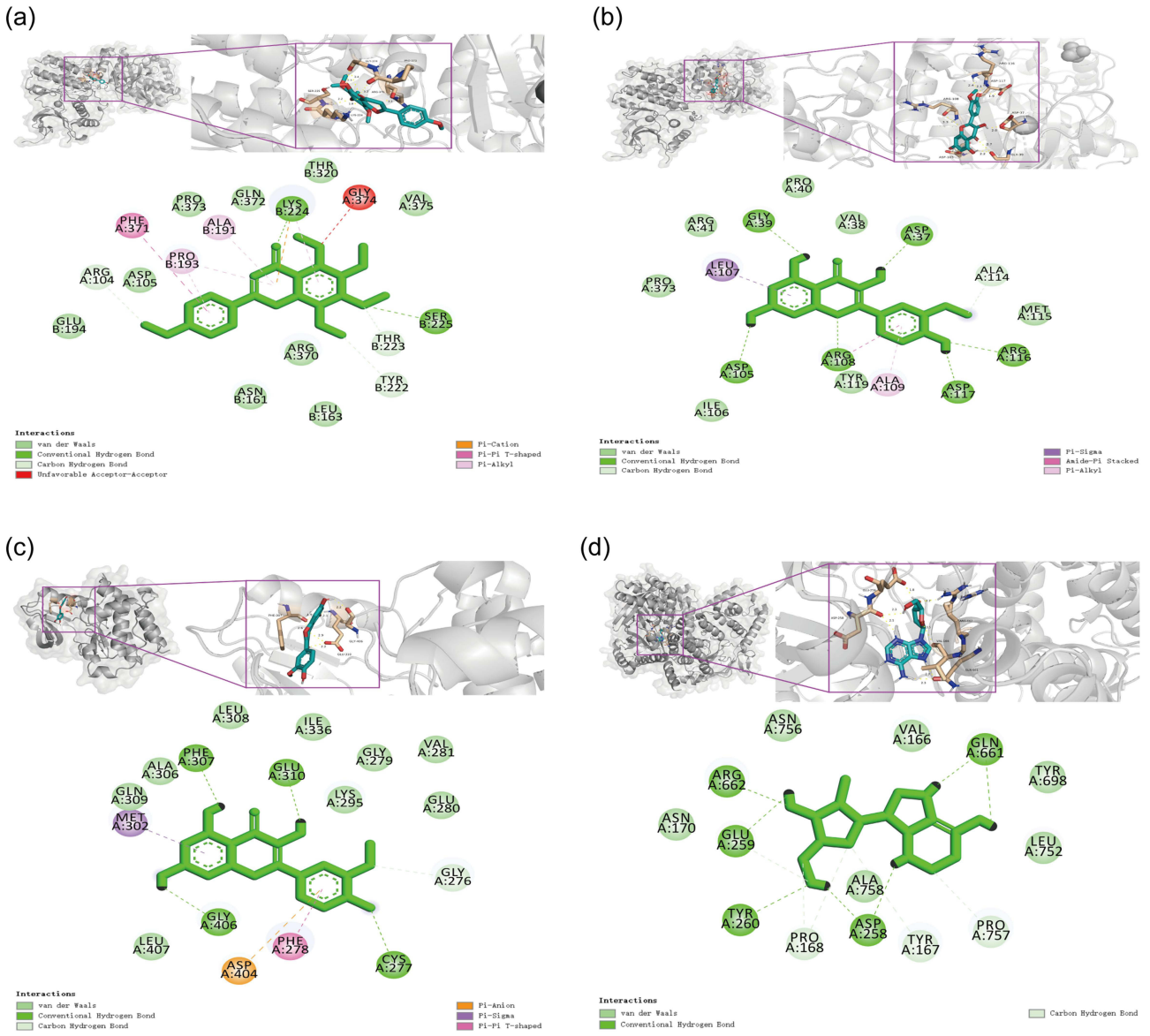

Figure 4 Molecular docking results. (**a**) Tangeritin binds with MAPK3; (**b**) Isorhamnetin binds with MAPK; (**c**) Isorhamnetin binds with SRC; (**d**) Adenosine binds with PIK3CA.

Stability Analysis of the Complex

Root Mean Square Deviation (RMSD) Analysis

RMSD is a crucial metric for evaluating the similarity of molecular mimicry or protein conformation to the target structure, providing a quantitative assessment of system stability by calculating the root-mean-square deviation of atomic positions. As shown in Figure 5a, the horizontal axis represents time, while the vertical axis represents the overall deviation values. The RMSD of small molecules, proteins, and complexes fluctuated during the initial phase but stabilized after 60 ns, indicating that the complexes gradually reached equilibrium.

Radius of Gyration (Rg) Analysis

Rg is used to describe changes in the overall structure and is an important measure of the compactness of a protein structure. Significant changes in Rg suggest an increase in the system's expansion. According to Figure 5b, the Rg value of the complex gradually stabilizes, indicating increasing stability in its overall structure.

Root Mean Square Fluctuation (RMSF) Analysis

RMSF reflects the degree of flexibility by calculating the root-mean-square fluctuation of each amino acid residue in a protein, serving as a key indicator of the local dynamics within the protein structure. As shown in Figure 5c, the horizontal axis represents the residues, while the vertical axis represents the fluctuation values. The peaks and valleys in the figure correspond to the maximum and minimum RMSF values, respectively. Residues at the peaks may exhibit higher flexibility and are more likely to undergo conformational changes or participate in interactions crucial for protein function. Conversely, residues at the troughs tend to be more stable Certain regions with higher RMSF values may be critical for protein function and could be involved in enzyme active sites, protein interaction interfaces, or in regulating conformational changes in the protein.

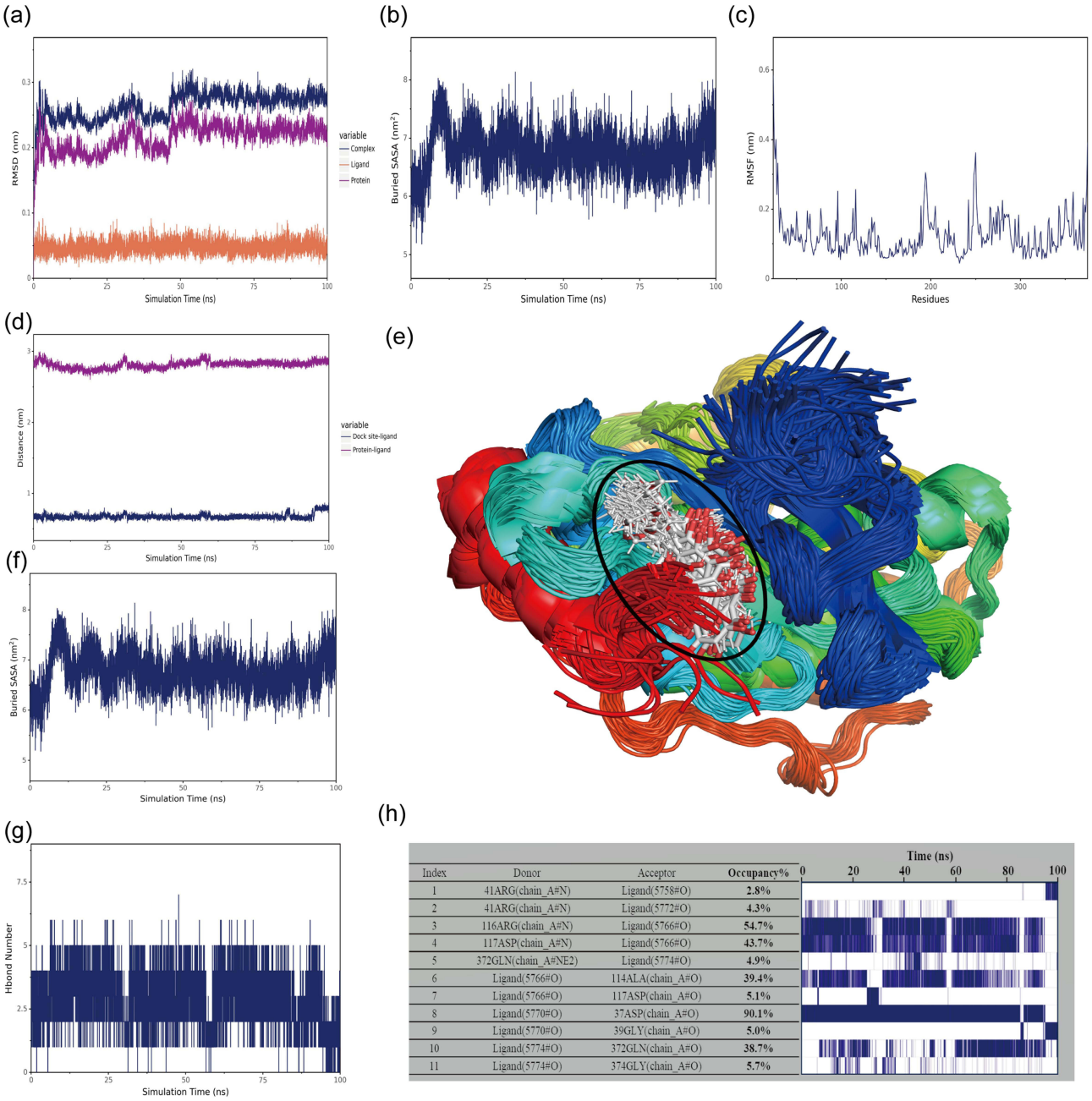

Index	Donor	Acceptor	Occupancy%
1	41ARG(chain_A#N)	Ligand(5758#O)	2.8%
2	41ARG(chain_A#N)	Ligand(5772#O)	4.3%
3	116ARG(chain_A#N)	Ligand(5766#O)	54.7%
4	117ASP(chain_A#N)	Ligand(5766#O)	43.7%
5	372GLN(chain_A#NE2)	Ligand(5774#O)	4.9%
6	Ligand(5766#O)	114ALA(chain_A#O)	39.4%
7	Ligand(5766#O)	117ASP(chain_A#O)	5.1%
8	Ligand(5770#O)	37ASP(chain_A#O)	90.1%
9	Ligand(5770#O)	39GLY(chain_A#O)	5.0%
10	Ligand(5774#O)	372GLN(chain_A#O)	38.7%
11	Ligand(5774#O)	374GLY(chain_A#O)	5.7%

Figure 5 Continued.

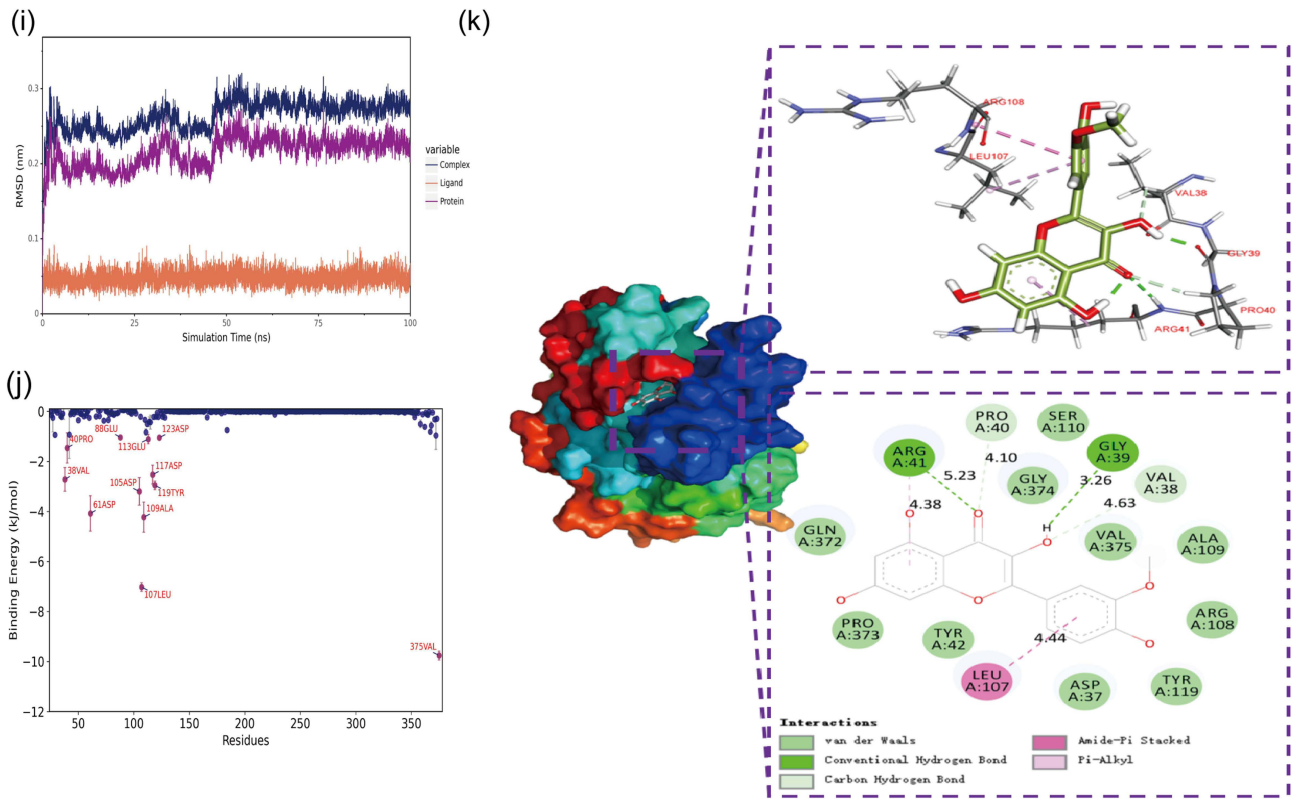

Figure 5 Molecular dynamics simulation results. (**a**) RMSD of the complex, protein, and small molecule ligand; (**b**) Rg of the complex; (**c**) RMSF of the protein in the complex; (**d**) Distance between the docking site and the small molecule on the protein surface; (**e**) Superimposed conformations in simulation. The black circle indicates the position of the small molecule's overlaid conformation. (**f**) Buried SASA; (**g**) Hbond number; (**h**) Occupancy; (**i**) VDW and ELE between the small molecule and the protein; (**j**) Amino acid contribution to binding energy; (**k**) Interactions between the protein and the small molecule.

Analysis of Small Molecule Binding Stability to the Protein

Centroid Evolution Analysis

To explore the behavior of the small molecule on the protein surface, the initial docking position of the small molecule was obtained, and the distance between the residue centroid at the initial docking site and the centroid of the small molecule was measured. Additionally, the distance between the small molecule and the entire protein centroid was analyzed. These distances help judge the binding of the small molecule to the protein. Data from Figure 5d shows that the distance between the small molecule and the protein, as well as with the initial binding site, remains stable throughout the simulation, indicating good stability of the binding. Notably, there was a slight fluctuation in the distance to the binding site towards the end of the simulation (95–100 ns), possibly reflecting minor adjustments in the binding site of the small molecule.

Analysis of Small Molecule Binding Sites

By superimposing the simulated conformations of the small molecule and the protein, it can be observed, as shown in Figure 5e, that the small molecule in the complex remains near the initial binding site with a high degree of overlap. This phenomenon indicates that the small molecule maintains a stable binding state with the protein throughout the simulation.

Analysis of Buried Solvent-Accessible Surface Area (Buried SASA)

Buried SASA reflects the size of the binding interface between the small molecule and the protein, revealing their binding state. Analysis of Buried SASA showed initial fluctuations, mainly due to conformational adjustments during the binding process of the small molecule to the protein. As shown in Figure 5f, the Buried SASA value gradually stabilizes as the simulation progresses, indicating that the small molecule reaches a stable binding state with the protein after conformational adjustments.

Analysis of Hydrogen Bond Interactions Between Small Molecule and Protein

Evolution of Hydrogen Bond Numbers

Hydrogen bonds are one of the key forces in the binding of proteins to ligands and are closely related to electrostatic interactions, thus reflecting the strength of electrostatic interactions. According to data in Figure 5g, the number of hydrogen bonds between the small molecule and the protein is relatively low and stable, generally maintained between 1 and 5. Additionally, a decrease in hydrogen bond numbers was observed towards the end of the simulation, indicating minor conformational adjustments in the small molecule during the binding process.

Analysis of Hydrogen Bond Occupancy (Frequency)

To gain a deeper understanding of which protein residues form hydrogen bonds with the small molecule and the stability of these hydrogen bonds, the occupancy (ie, the frequency of hydrogen bond formation) of hydrogen bonds between the small molecule and the protein was analyzed. As shown in Figure 5h, the left side lists the acceptors, donors, and their occupancy rates, while the right side shows the formation frequency of the corresponding hydrogen bonds, with the density of the lines reflecting the frequency of hydrogen bond formation. The graph indicates that the hydrogen bonds formed between the small molecule and the protein generally show high stability, particularly bonds such as those between Ligand and 37ASP, 116ARG and Ligand, 117ASP and Ligand.

Interaction Analysis of Small Molecule Binding to Protein

Analysis of Electrostatic and Van der Waals Interactions

Ignoring solvation effects, the Van der Waals forces (VDW) and electrostatic interaction forces (ELE) between the small molecule and the protein in the complex were calculated, and their changes during the simulation were analyzed. VDW represents Van der Waals interaction forces, ELE represents electrostatic interactions, and the Binding value, which is the sum of VDW and ELE, is used to represent the binding energy of the small molecule to the protein without considering solvation effects. According to data in Figure 5i, VDW and ELE in the complex gradually stabilize during the simulation, reflecting the stable binding between the small molecule and the protein.

Binding Energy Analysis

Considering solvation energy, a comprehensive analysis of parameters such as RMSD, Rg, Distance, Buried SASA, and interaction energy was conducted, and a trajectory of the complex in a stable state was selected. Molecular Mechanics-Poisson Boltzmann Surface Area (MM-PBSA) was applied to calculate related energy terms of binding energy. Results are shown in the table: ΔE_{ele} represents the electrostatic interaction energy between the small molecule and the protein, ΔE_{vdw} represents the Van der Waals interaction energy, ΔE_{pol} represents polar solvation energy, ie, electrostatic potential energy, and ΔE_{nonpol} represents nonpolar solvation energy, indicating hydrophobic interactions. ΔE_{MMPBSA} is the sum of these energy terms, and ΔG_{bind} is the sum of ΔE_{MMPBSA} and -TΔS (since the calculation of -TΔS has a high degree of uncertainty, it is usually not considered in the comparison of binding energies, and ΔE_{MMPBSA} is directly used to represent binding energy). According to the analysis in Table 5, the Van der Waals interaction ΔE_{vdw} in the complex is significantly higher than the electrostatic interaction ΔE_{ele} and the hydrophobic interaction ΔE_{nonpol}, with ΔE_{vdw} being five times that of ΔE_{ele} and 8.4 times that of ΔE_{nonpol}. This indicates that Van der Waals forces are the dominant forces, electrostatic interactions play a secondary role, and hydrophobic interactions are complementary. Therefore, the binding energy of the small molecule to the protein is high, showing strong affinity.

Residue Contribution Analysis

By decomposing the binding energy ΔE_{MMPBSA}, the contribution of each amino acid residue to the total binding energy was analyzed, thus assessing key amino acids in the protein. As shown in Figure 5j, residues that contribute significantly to the overall

Table 5 Binding Energy and Its Components at Stable State (Unit: kJ/Mol)

Complex	ΔE_{vdw}	ΔE_{ele}	ΔE_{pol}	ΔE_{nonpol}	ΔE_{MMPBSA}	-TΔS	ΔG_{bind}*
Protein-ligand	−156.673±0.68	−31.57±0.916	153.003±3.575	−18.506±0.238	−53.745±3.871	25.293±1.34	−28.452±2.608

Notes: *$\Delta G_{bind}=\Delta E_{vdw}+\Delta E_{ele}+\Delta E_{pol}+\Delta E_{nonpol}$-T$\Delta$S.

binding energy include 375VAL, 107LEU, 61ALA, 119TYR, among others. These residues are key amino acids in the binding of the small molecule and play a significant role in maintaining the stable binding between the small molecule and the protein.

Structural Analysis

The last frame of the simulation was selected for structural and interaction analysis. As shown in Figure 5k, ARG41 and GLY39 in the protein form hydrogen bonds with the small molecule. Additionally, PRO40 and VAL38 form carbon-hydrogen bond interactions with the small molecule, while ILE107 forms two types of hydrophobic interactions with the small molecule: Pi-Alkyl and Amide-Pi Stacked. Meanwhile, PRO373, TYR42, VAL375, TYR119, and other amino acids engage in Van der Waals interactions with the small molecule, collectively maintaining the stable binding of the small molecule to the protein.

Animal Experiment Validation Results for ZJP Treatment of PLGC

Improvement of General Conditions in PLGC Rats by ZJP

Before establishing the PLGC rat model, there was no significant difference in body mass among the groups ($P>0.05$). As the modeling time increased, compared to the normal group, the model rats showed a gradual reduction in body weight ($P<0.01$) and exhibited symptoms such as dull fur, reduced eating, and decreased activity. After drug intervention, compared to the model group, rats in the ZJP and Vitacoenzyme groups showed improvements in body weight, eating habits, and overall vitality to varying degrees ($P<0.01$), with the high-dose ZJP group showing the most significant improvement ($P<0.01$) (Figure 6).

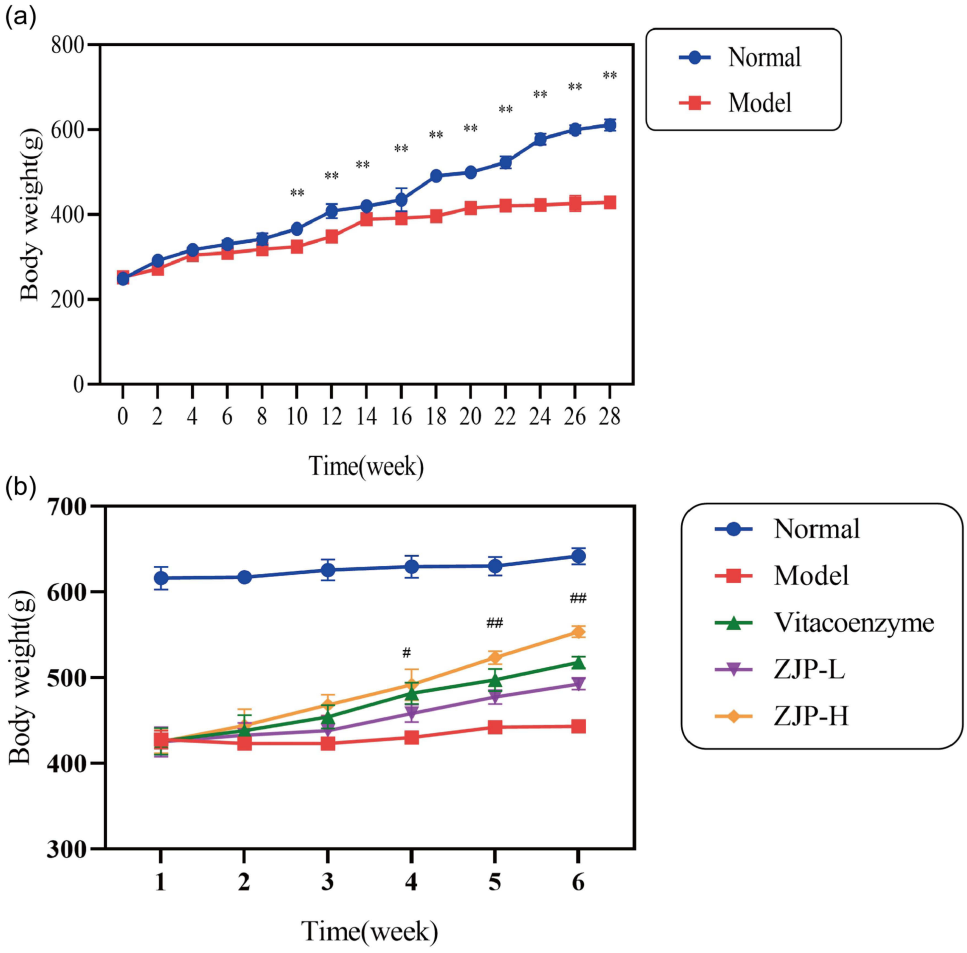

Figure 6 Effects of ZJP on Body Weight of PLGC Rats (mean ± SD, n=8). **compared to normal group ($P<0.01$); #compared to model group ($P<0.05$); ##compared to model group ($P<0.01$). (**a**) Changes in rat body weight during model establishment; (**b**) Changes in rat body weight during drug treatment period.

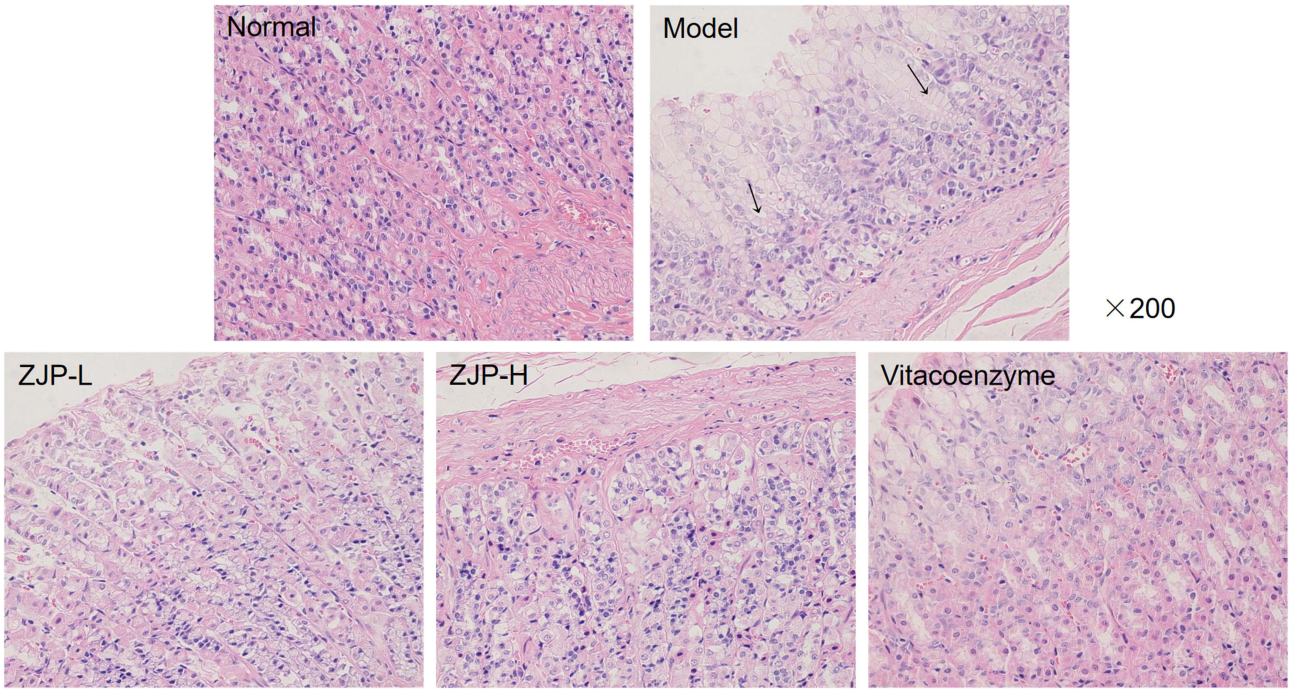

Figure 7 HE staining of gastric tissue in Normal, Model, ZJP-L, ZJP-H, and Vitacoenzyme groups (×200, mean ± SD, n=8).

Effects of ZJP on Gastric Tissue Pathology in PLGC Rats

In the normal group, the gastric mucosa was clear, the mucosal glands were abundant and tightly arranged, and there was no infiltration of inflammatory cells. In the model group, there were observable losses of epithelial cells, thinning of the gastric mucosal layer, reduction in the number of intrinsic glands, and in some areas, intestinal metaplasia and infiltration of inflammatory cells were visible. After treatment with ZJP and Vitacoenzyme, all groups showed significant improvement in gastric mucosal damage. The ZJP-L group still had some damage and inflammatory signs, whereas the ZJP-H and Vitacoenzyme groups showed relatively organized gland structures, less infiltration of inflammatory cells, more normal cell morphology, and improved mucosal lesions without any goblet cells (see Figure 7).

Impact of ZJP on Gastric Tissue Cytokine Levels in PLGC Rats

Compared to the normal group, the model group showed significantly increased levels of inflammatory cytokines TNF-α and IL-6 in gastric tissues ($P<0.01$). Compared to the model group, all treatment groups showed a significant reduction in TNF-α and IL-6 levels ($P<0.01$), with the ZJP-H group showing the most pronounced effects (see Figure 8a–c).

Changes in p-MEK1, p-ERK1/2, Ratios of p-MEK1/MEK1, p-ERK1/2/ERK1/2 and c-Myc Protein Levels in Gastric Tissues of Different Groups

Figure 8d–i shows Western-blot images of p-MEK1, p-ERK1/2, Ratios of p-MEK1/MEK1, p-ERK1/2/ERK1/2 and c-myc proteins in the normal, model, Vitacoenzyme, low-dose ZJP, and high-dose ZJP groups. Compared to the normal group, the expression of p-MEK1 and p-ERK1/2 was significantly upregulated in the model group's gastric tissues ($P<0.01$). After drug intervention, the levels of p-MEK1/MEK1, p-ERK1/2/ERK1/2 decreased ($P<0.05$), with the most significant reduction in the high-dose ZJP group ($P<0.01$). Additionally, compared to the normal group, the level of c-myc protein in the gastric tissues of the model group was significantly elevated ($P<0.01$). Compared to the model group, all treatment groups showed a significant decrease in c-myc protein levels in gastric tissues ($P<0.01$), with the ZJP-H group showing the most pronounced effects.

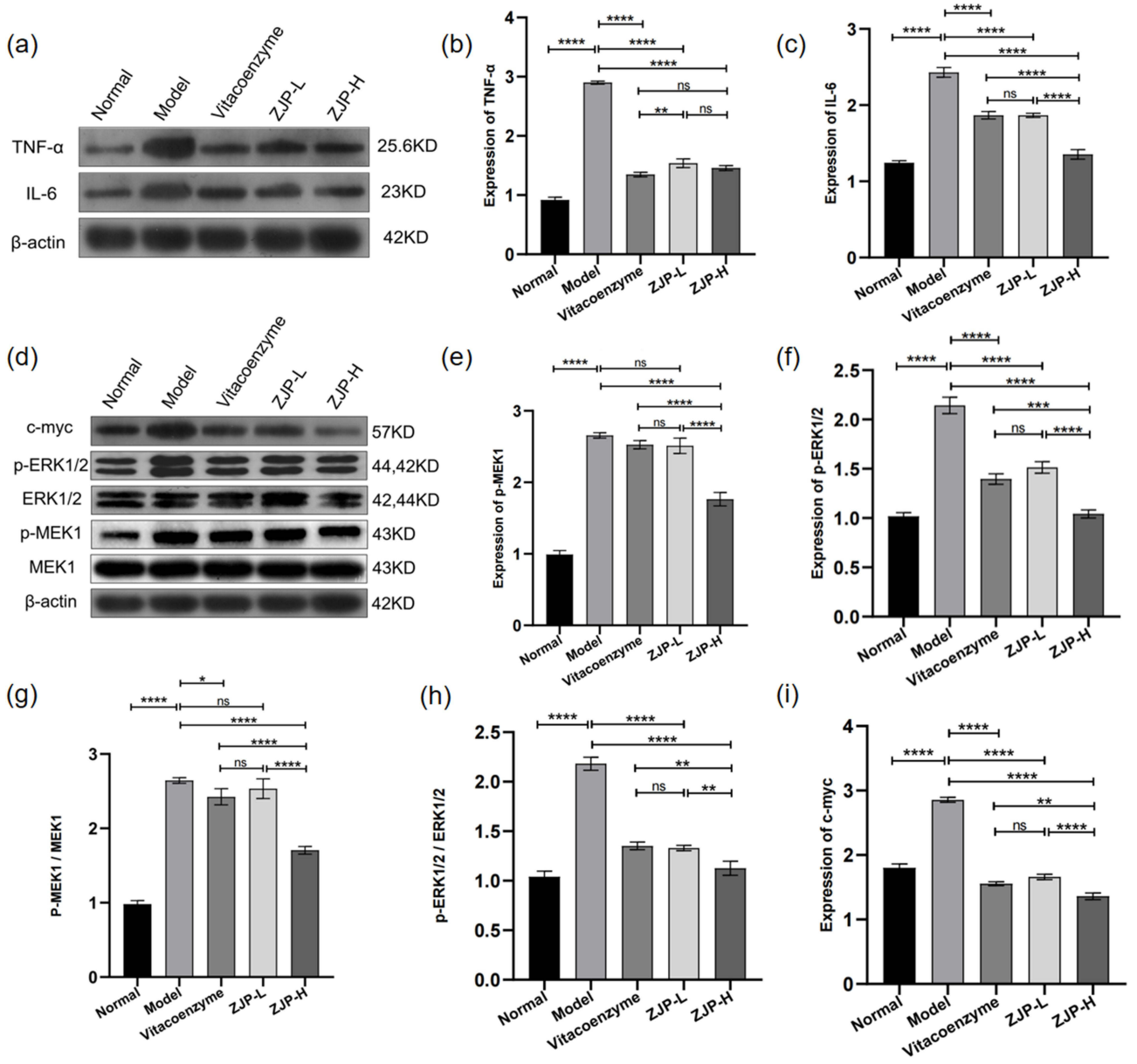

Figure 8 Changes in TNF-α, IL-6, MEK1, p-MEK1, ERK1/2, p-ERK1/2 and c-myc levels in gastric tissues of different groups (mean ± SD, n=8). (**a**) Representative Western blot images of the TNF-αand IL-6 levels; (**b** and **c**) Quantification of the TNF-αand IL-6 levels; (**d**) Representative Western blot images of the MEK1, p-MEK1, ERK1/2, p-ERK1/2 and c-myc levels; (**e-i**) Quantification of the p-MEK1, p-ERK1/2, p-MEK1/MEK1, p-ERK1/2 / ERK1/2 and c-myc levels. **** $P < 0.0001$; *** $P < 0.001$; ** $P < 0.01$; * $P < 0.05$; ns $P > 0.05$.

Discussion

Network pharmacology elucidates the mechanism of drugs through the intersection and interaction of multi-dimensional targets, aligning well with the holistic view of traditional Chinese medicine. Combined with modern pharmacological techniques such as liquid chromatography-mass spectrometry (LC-MS), it enables more accurate assessment of the rationality and interaction of traditional Chinese medicine. This study leverages LC-MS and network pharmacology to thoroughly explore the anti-inflammatory, anti-cancer factors, and signaling pathways influenced by ZJP in PLGC. Molecular docking and molecular dynamics simulation techniques further verify the spatial and energy match between targets and components, providing a theoretical basis for the core components of ZJP in reversing PLGC, and corroborating the effective components' role in improving PLGC through in vivo experiments.

This research, utilizing LC-MS and network pharmacology, identifies active components in ZJP such as Tangeritin, Isorhamnetin, Caffeic acid, Azelaic acid, and Adenosine as the main pharmacologically active components for treating PLGC.

Tangeritin, for instance, can inhibit inflammation and extracellular matrix degradation in cartilage cells and animal models through the Nrf2/NF-κB and MAPK/NF-κB pathways, used to treat osteoarthritis.[41] Isorhamnetin, widely found in fruits and herbs, has high pharmacological activity,[42] significantly inhibiting platelet aggregation induced by collagen and TRAP-6, thereby protecting the cardiovascular system and preventing related diseases.[43,44] It also affects cytokines and kinase expressions by regulating pathways like PI3K/Akt/PKB, NF-κB, and MAPK, conferring anti-inflammatory, antioxidant, organ-protective, and anti-obesity effects.[42] It can inhibit tumor cell proliferation and induce apoptosis by modulating tumor suppressor genes, oncogenes, and signaling pathways,[45] showing anti-tumor activity against gastric cancer, liver cancer, and colorectal cancer.[46–48] Caffeic acid, a naturally occurring phytochemical, has been proven to possess robust antimicrobial properties.[49] Several studies demonstrate that these main active components exhibit varying degrees of anti-inflammatory, antioxidant, and anti-cancer effects.[50–54] Molecular dynamics simulations have shown that Isorhamnetin binds stably at the initial binding site, forming numerous hydrogen bonds with MAPK3, indicating high overall stability. The Gibbs free energy of binding between the two is −28.452±2.608 kJ/mol, suggesting a high affinity of Isorhamnetin for MAPK3. In the complex, Van der Waals interactions play a dominant role over electrostatic and hydrophobic interactions, supporting its potential as a key pharmacologically active component of ZJP for treating PLGC.

Topological analysis of the PPI diagram identified core targets such as PIK3R1, MAPK3, SRC, JAK2, STAT3, and PIK3CA in the prevention and treatment of PLGC by ZJP. Coupled with molecular docking and dynamics, it is suggested that MAPK3 has the best affinity with the main pharmacological components and is part of the MAPK/ERK signaling pathway, aligning with KEGG enrichment analysis results, making it a potential significant target and pathway in the treatment of PLGC. The MAPK pathway, or mitogen-activated protein kinase, is a crucial signaling pathway widely present in various human cells. The MAPK protein family plays an important role in regulating intracellular gene transcription and protein expression, affecting physiological processes like cell proliferation, differentiation, and apoptosis. It is closely associated with cancer, involved in the onset and development of various tumors such as colorectal cancer, lung cancer, cervical cancer, gastric cancer, hypertension, non-ossifying fibromas, ovarian tumors, rectal cancer, neuroblastoma, nasopharyngeal carcinoma, and renal cysts. Activation of MAPK proteins in these diseases often impacts cell functions, potentially a crucial pathogenic mechanism.[55] As a classical pathway for GC and PLGC, the MAPK/ERK signaling pathway primarily follows this sequence: Ras→activates Raf→activates MEK→activates ERK1/2→activates RSK or transcription factors to produce biological effects (as shown in Figure 9), which

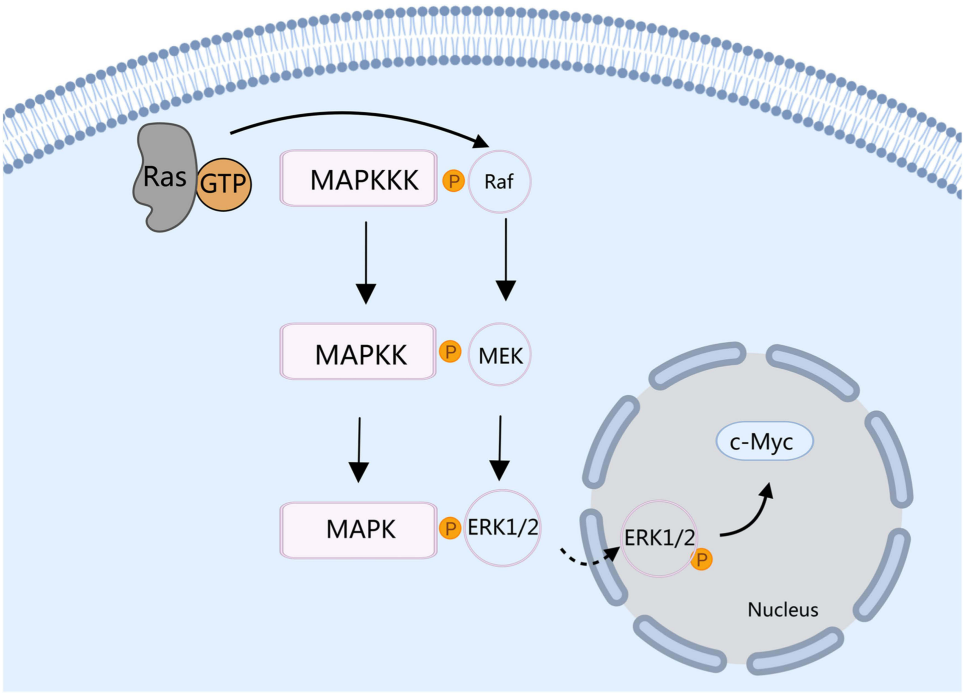

Figure 9 MAPK/MEK/ERK signaling pathway.

can be activated upstream by growth factors and downstream can regulate nuclear transcription factors like c-fos, Elk-1, c-myc, etc., thereby participating in inflammatory responses and cell proliferation, playing a significant role in the development of gastric cancer.[56] Previous studies have shown that activation of the MAPK/ERK pathway is involved in TGF-β1-induced epithelial-mesenchymal transition (EMT),[57] now included in molecular targeted therapy studies for gallbladder cancer.[58] An animal study confirmed that inhibiting the pERK1/2 signal in a gastric inflammation model created in C57BL/6 mice with ethanol can reduce MMP-10 expression induced by ethanol in gastric inflammation, improve gastric mucosal damage, and alleviate inflammatory responses.[59] Studies have also observed significantly increased activation of STAT3 and ERK in Helicobacter pylori-dependent gastritis, with the expression of pro-inflammatory cytokines activated by the STAT3 and ERK pathways related to the progression of GC.[60] Multiple studies confirm that inhibiting the ERK pathway displays strong anti-inflammatory activity,[61,62] and down-regulating ERK1/2 and PI3K/Akt signal pathways to suppress tumor activity by expressing RhoA/MMP-9,[63] with tMMP9 as a secreted protein playing an important role in local proteolysis of the extracellular matrix, participating in promoting neutrophil-mediated gastric tissue inflammatory responses.[64] c-Myc, a downstream protein of the ERK pathway, is one of the first oncogene products discovered related to tumor cell proliferation and apoptosis, capable of malignant transformation. It binds with DNA in the nucleus to promote protein expression, leading to cell growth; it can also act as a regulatory protein, controlling the transition of cells from G0/G1 to S phase, and regulating cell proliferation and apoptosis, playing a significant role in the transformation from normal cell growth to tumor growth.[65,66] Experimental results show that the expression rate of C-myc increases progressively from groups with atrophic gastritis, superficial gastritis, gastric ulcers, to gastric cancer groups, suggesting that high expression of the C-myc gene might lead to cell apoptosis.[67] Additional studies have shown that over 61% of patients with gastric cancer have significantly higher levels of ERK than normal individuals,[68] and the abnormal signaling pathway of MEK/ERK/c-myc is closely linked to the proliferation and apoptosis of gastric cancer cells. Further observation revealed that the overactivation of the MEK/ERK/c-myc pathway plays a key role in tumor onset and development, not only regulating the cancer process but also controlling the invasive capabilities and metastatic behavior of tumor cells.[69] By inhibiting this pathway, it is possible to stop the proliferation of gastric cancer cells and promote apoptosis, interrupting the malignant cycle of tumor cell growth and survival, providing new targets and directions for treatment.

Thus, this study further used Western Blot to examine key indicators on the MAPK/ERK signaling pathway and downstream c-myc protein and inflammatory cytokines TNF-α, IL-6 expressions. Results indicate that ZJP can significantly inhibit the activation of the MEK/ERK/c-myc pathway, downregulate the expression of inflammatory cytokines TNF-α, IL-6 in gastric tissues, improve local symptoms of the gastric mucosa, and reverse PLGC. The findings of ZJP's reversal effects on PLGC suggest that traditional Chinese medicine holds certain advantages in the early prevention and treatment of malignant diseases, providing new insights and methods for treating pre-cancerous gastric lesions with traditional Chinese medicine, and offering new experimental evidence for the clinical application of ZJP, expanding the research field of modernization of traditional Chinese medicine.

However, this study still has certain limitations. First, although the main pharmacologically active components in ZJP were explored using LC-MS, there is still a lack of experimental validation of the exact therapeutic effects of individual components, and further cell experiments are needed to improve the level of evidence. Second, as a clinically applicable drug, ZJP should undergo related clinical trials in the future to increase its evidence base. Due to certain limitations, we were unable to validate the MAPK and PI3K-AKT pathways in this study. These pathways will also be an area of focus for us in subsequent studies. Lastly, ZJP could serve as a promising therapeutic agent for early intervention in human gastric lesions. Future clinical studies are needed to further validate its efficacy, safety, and optimal dosage, supporting the application of ZJP in gastric cancer prevention and advancing the modernization of traditional Chinese medicine in oncology.

Conclusion

ZJP can significantly improve the pathological damage in gastric tissues of rats with MNNG-induced PLGC, and reduce the levels of cytokines IL-6 and TNF-α, achieving a reversal effect on PLGC. The mechanism is likely related to the inhibition of the MEK/ERK/c-Myc pathway and the regulation of cell proliferation and apoptosis. These interactions have been validated through network pharmacology and animal experiments. These findings not only provide a new drug candidate for the clinical management of PLGC, but also highlight an avenue of the potential for ZJP as a therapeutic agent in human gastric lesions.

Institutional Review Board Statement

All the animal studies were performed in accordance with the National Institutes of Health Guide for the Care and Use of Laboratory Animals, and were approved by the Experimental Animal Ethics Committee of Shaanxi University of Chinese Medicine (No. SUCMDL20220602001-1).

Abbreviations

PLGC, precancerous lesions gastric cancer; GC, gastric cancer; ZJP, zuojin pill; HL, Rhizoma Coptidis, Huanglian; WZY, Fructus Evodiae, Wuzhuyu; UPLC-Q-Orbitrap HRMS, ultra-high performance liquid chromatography-quadrupole/electrostatic orbitrap high-resolution mass spectrometry; IM, intestinal metaplasia; Dys, dysplesa; CAG, chronic atrophic gastritis; HP, Helicobacter pylori; TCM, traditional Chinese medicine; PPI, protein–protein interaction; GO, Gene Ontology; KEGG, Kyoto Encyclopedia of Genes and Genomes; MNNG, N-Methyl-N'-nitro-N-nitrosoguanidine; DC, degree centrality; BC, betweenness centrality; CC, closeness centrality; EC, eigenvector centrality; LAC, local average connectivity-based method; NC, network centrality; MF, molecular function; BP, biological process; CC, cellular component; RMSD, Root mean square deviation; Rg, Radius of Gyration; RMSF, Root mean square fluctuation; buried SASA, buried solvent-accessible surface area.

Data Sharing Statement

The raw data supporting the conclusions of this manuscript will be available from the corresponding author on reasonable request.

Ethical Approval

This study is involving human data from public databases DrugBank, GeneCards, TTD, PharmGkb and OMIM. The ethics committee of The Affiliated Hospital of Shaanxi University of Traditional Chinese Medicine has approved this study (Supplementary 3).

Acknowledgments

This work was supported by the Education Department of Shaanxi Provincial Government (Grant No. 21JS011); the Department of Science and Technology of Shaanxi Province (No. 2022JM-457); Key Scientific Research Program of Shaanxi Provincial Department of Education (23JS013) and the Shaanxi Key Laboratory of Research on TCM Physical Constitution and Diseases Prevention and Treatment ([2012] No.1).

Author Contributions

All authors made a significant contribution to the work reported, whether that is in the conception, study design, execution, acquisition of data, analysis and interpretation, or in all these areas; took part in drafting, revising, or critically reviewing the article; gave final approval of the version to be published; have agreed on the journal to which the article has been submitted; and agree to be accountable for all aspects of the work.

Disclosure

The authors declare no competing interests in this work.

References

1. Sung H, Ferlay J, Siegel RL, et al. Global cancer statistics 2020: GLOBOCAN estimates of incidence and mortality worldwide for 36 Cancers in 185 countries. *CA Cancer J Clin*. 2021;71(3):209–249. doi:10.3322/caac.21660
2. Whiting JL, Sigurdsson A, Rowlands DC, et al. The long term results of endoscopic surveillance of premalignant gastric lesions. *Gut*. 2002;50(3):378–381. doi:10.1136/gut.50.3.378
3. Sipponen P, Maaroos HI. Chronic gastritis. *Scand J Gastroenterol*. 2015;50(6):657–667. doi:10.3109/00365521.2015.1019918
4. Song H, Ekheden IG, Zheng Z, et al. Incidence of gastric cancer among patients with gastric precancerous lesions: observational cohort study in a low risk Western population. *BMJ*. 2015;351:h3867. doi:10.1136/bmj.h3867
5. Wong BC, Lam SK, Wong WM, et al. Helicobacter pylori eradication to prevent gastric cancer in a high-risk region of China: a randomized controlled trial. *JAMA*. 2004;291(2):187–194. doi:10.1001/jama.291.2.187

6. Choi IJ, Kook MC, Kim YI, et al. Helicobacter pylori therapy for the prevention of metachronous gastric cancer. *N Engl J Med*. 2018;378(12):1085–1095. doi:10.1056/NEJMoa1708423
7. Huang RJ, Laszkowska M, In H, et al. Controlling gastric cancer in a world of heterogeneous risk. *Gastroenterology*. 2023;164(5):736–751. doi:10.1053/j.gastro.2023.01.018
8. Liou JM, Jiang XT, Chen CC, et al. Second-line levofloxacin-based quadruple therapy versus bismuth-based quadruple therapy for Helicobacter pylori eradication and long-term changes to the gut microbiota and antibiotic resistome: a multicentre, open-label, randomised controlled trial. *Lancet Gastroenterol Hepatol*. 2023;8(3):228–241. doi:10.1016/s2468-1253(22)00384-3
9. Lee JW, Kim N, Choi SI, et al. Prevalence and trends of multiple antimicrobial resistance of Helicobacter pylori in one tertiary hospital for 20 years in Korea. *Helicobacter*. 2023;28(1):e12939. doi:10.1111/hel.12939
10. Lu L, Wang Y, Ye J, et al. Quadruple therapy with vonoprazan 20 mg daily as a first-line treatment for Helicobacter pylori infection: a single-center, open-label, noninferiority, randomized controlled trial. *Helicobacter*. 2023;28(1):e12940. doi:10.1111/hel.12940
11. Wang Y, Chu F, Lin J, et al. Erianin, the main active ingredient of Dendrobium chrysotoxum Lindl, inhibits precancerous lesions of gastric cancer (PLGC) through suppression of the HRAS-PI3K-AKT signaling pathway as revealed by network pharmacology and in vitro experimental verification. *J Ethnopharmacol*. 2021;279:114399. doi:10.1016/j.jep.2021.114399
12. Canzian F, Rizzato C, Obazee O, et al. Genetic polymorphisms in the cag pathogenicity island of Helicobacter pylori and risk of stomach cancer and high-grade premalignant gastric lesions. *Int J Cancer*. 2020;147(9):2437–2445. doi:10.1002/ijc.33032
13. Cover TL, Lacy DB, Ohi MD. The helicobacter pylori Cag Type IV secretion system. *Trends Microbiol*. 2020;28(8):682–695. doi:10.1016/j.tim.2020.02.004
14. Group ES. Risk factors for atrophic chronic gastritis in a European population: results of the Eurohepygast study. *Gut*. 2002;50(6):779–785. doi:10.1136/gut.50.6.779
15. Thrift AP, Wenker TN, El-Serag HB. Global burden of gastric cancer: epidemiological trends, risk factors, screening and prevention. *Nat Rev Clin Oncol*. 2023;20(5):338–349. doi:10.1038/s41571-023-00747-0
16. Li Z, Feiyue Z, Gaofeng L. Traditional Chinese medicine and lung cancer–From theory to practice. *Biomed Pharmacother*. 2021;137:111381. doi:10.1016/j.biopha.2021.111381
17. Zhang X, Qiu H, Li C, et al. The positive role of traditional Chinese medicine as an adjunctive therapy for cancer. *Biosci Trends*. 2021;15(5):283–298. doi:10.5582/bst.2021.01318
18. Xu W, Li B, Xu M, et al. Traditional Chinese medicine for precancerous lesions of gastric cancer: a review. *Biomed Pharmacother*. 2022;146:112542. doi:10.1016/j.biopha.2021.112542
19. Wang J, Zhang T, Zhu L, et al. Anti-ulcerogenic effect of Zuojin Pill against ethanol-induced acute gastric lesion in animal models. *J Ethnopharmacol*. 2015;173:459–467. doi:10.1016/j.jep.2015.04.017
20. Xiong M, Chen X, Wang H, et al. Combining transcriptomics and network pharmacology to reveal the mechanism of Zuojin capsule improving spasmolytic polypeptide-expressing metaplasia. *J Ethnopharmacol*. 2024;318(Pt B):117075. doi:10.1016/j.jep.2023.117075
21. Zheng S, Xue T, Wang B, et al. Chinese medicine in the treatment of ulcerative colitis: the mechanisms of signaling pathway regulations. *Am J Chin Med*. 2022;50(7):1781–1798. doi:10.1142/s0192415x22500756
22. Wang T, Yan YF, Yang L, et al. Effects of Zuojin pill on depressive behavior and gastrointestinal function in rats with chronic unpredictable mild stress: role of the brain-gut axis. *J Ethnopharmacol*. 2020;254:112713. doi:10.1016/j.jep.2020.112713
23. Song D, Hao J, Fan D. Biological properties and clinical applications of berberine. *Front Med*. 2020;14(5):564–582. doi:10.1007/s11684-019-0724-6
24. Yarla NS, Bishayee A, Sethi G, et al. Targeting arachidonic acid pathway by natural products for cancer prevention and therapy. *Semin Cancer Biol*. 2016;40–41:48–81. doi:10.1016/j.semcancer.2016.02.001
25. Liu X, Zhang N, Liu Y, et al. MPB, a novel berberine derivative, enhances lysosomal and bactericidal properties via TGF-β-activated kinase 1-dependent activation of the transcription factor EB. *FASEB j*. 2019;33(1):1468–1481. doi:10.1096/fj.201801198R
26. Hesari A, Ghasemi F, Cicero AFG, et al. Berberine: a potential adjunct for the treatment of gastrointestinal cancers? *J Cell Biochem*. 2018;119(12):9655–9663. doi:10.1002/jcb.27392
27. Tian KM, Li JJ, Xu SW. Rutaecarpine: a promising cardiovascular protective alkaloid from Evodia rutaecarpa (Wu Zhu Yu). *Pharmacol Res*. 2019;141:541–550. doi:10.1016/j.phrs.2018.12.019
28. Huang CJ, Huang WC, Lin WT, et al. Rutaecarpine, an alkaloid from evodia rutaecarpa, can prevent platelet activation in humans and reduce microvascular thrombosis in mice: crucial role of the PI3K/Akt/GSK3βSignal axis through a cyclic nucleotides/VASP-independent mechanism. *Int J Mol Sci*. 2021;22(20):11109. doi:10.3390/ijms222011109
29. Ye C, Zhang N, Zhao Q, et al. Evodiamine alleviates lipopolysaccharide-induced pulmonary inflammation and fibrosis by activating apelin pathway. *Phytother Res*. 2021;35(6):3406–3417. doi:10.1002/ptr.7062
30. Yu L, Wang Z, Huang M, et al. Evodia alkaloids suppress gluconeogenesis and lipogenesis by activating the constitutive androstane receptor. *Biochim Biophys Acta*. 2016;1859(9):1100–1111. doi:10.1016/j.bbagrm.2015.10.001
31. Jiang J, Hu C. Evodiamine: a novel anti-cancer alkaloid from Evodia rutaecarpa. *Molecules*. 2009;14(5):1852–1859. doi:10.3390/molecules14051852
32. Tong Y, Wang R, Liu X, et al. Zuojin Pill ameliorates chronic atrophic gastritis induced by MNNG through TGF-β1/PI3K/Akt axis. *J Ethnopharmacol*. 2021;271:113893. doi:10.1016/j.jep.2021.113893
33. Wen J, Wu S, Ma X, et al. Zuojin Pill attenuates Helicobacter pylori-induced chronic atrophic gastritis in rats and improves gastric epithelial cells function in GES-1 cells. *J Ethnopharmacol*. 2022;285:114855. doi:10.1016/j.jep.2021.114855
34. Wang K, Miao X, Kong F, et al. Integrating network pharmacology and experimental verification to explore the mechanism of effect of Zuojin Pills in pancreatic cancer treatment. *Drug Des Devel Ther*. 2021;15:3749–3764. doi:10.2147/dddt.S323360
35. Guo W, Huang J, Wang N, et al. Integrating network pharmacology and pharmacological evaluation for deciphering the action mechanism of herbal formula Zuojin Pill in suppressing hepatocellular carcinoma. *Front Pharmacol*. 2019;10:1185. doi:10.3389/fphar.2019.01185
36. Fan JH, Xu MM, Zhou LM, et al. Integrating network pharmacology deciphers the action mechanism of Zuojin capsule in suppressing colorectal cancer. *Phytomedicine*. 2022;96:153881. doi:10.1016/j.phymed.2021.153881

37. Zaman Z, Khan S, Nouroz F, et al. Targeting protein tyrosine phosphatase to unravel possible inhibitors for Streptococcus pneumoniae using molecular docking, molecular dynamics simulations coupled with free energy calculations. *Life Sci*. 2021;264:118621. doi:10.1016/j.lfs.2020.118621
38. Yang R, Liu H, Bai C, et al. Chemical composition and pharmacological mechanism of Qingfei Paidu Decoction and Ma Xing Shi Gan Decoction against coronavirus disease 2019 (COVID-19): in silico and experimental study. *Pharmacol Res*. 2020;157:104820. doi:10.1016/j.phrs.2020.104820
39. Chu F, Li Y, Meng X, et al. Gut microbial dysbiosis and changes in fecal metabolic phenotype in precancerous lesions of gastric cancer induced with N-Methyl-N'-Nitro-N-Nitrosoguanidine, Sodium Salicylate, Ranitidine, and irregular diet. *Front Physiol*. 2021;12:733979. doi:10.3389/fphys.2021.733979
40. Wang XY, Wang LL, Zheng X, et al. Expression of p-STAT3 and vascular endothelial growth factor in MNNG-induced precancerous lesions and gastric tumors in rats. *World J Gastrointest Oncol*. 2016;8(3):305–313. doi:10.4251/wjgo.v8.i3.305
41. Shi Y, Chen J, Li S, et al. Tangeretin suppresses osteoarthritis progression via the Nrf2/NF-κB and MAPK/NF-κB signaling pathways. *Phytomedicine*. 2022;98:153928. doi:10.1016/j.phymed.2022.153928
42. Gong G, Guan YY, Zhang ZL, et al. Isorhamnetin: a review of pharmacological effects. *Biomed Pharmacother*. 2020;128:110301. doi:10.1016/j.biopha.2020.110301
43. Rodríguez L, Badimon L, Méndez D, et al. Antiplatelet activity of isorhamnetin via mitochondrial regulation. *Antioxidants*. 2021;10(5):666. doi:10.3390/antiox10050666
44. Xu Y, Tang C, Tan S, et al. Cardioprotective effect of isorhamnetin against myocardial ischemia reperfusion (I/R) injury in isolated rat heart through attenuation of apoptosis. *J Cell Mol Med*. 2020;24(11):6253–6262. doi:10.1111/jcmm.15267
45. Hu J, Zhang Y, Jiang X, et al. ROS-mediated activation and mitochondrial translocation of CaMKII contributes to Drp1-dependent mitochondrial fission and apoptosis in triple-negative breast cancer cells by isorhamnetin and chloroquine. *J Exp Clin Cancer Res*. 2019;38(1):225. doi:10.1186/s13046-019-1201-4
46. Li C, Li J, Li Y, et al. Isorhamnetin promotes MKN-45 gastric cancer cell apoptosis by inhibiting PI3K-mediated adaptive autophagy in a hypoxic environment. *J Agric Food Chem*. 2021;69(29):8130–8143. doi:10.1021/acs.jafc.1c02620
47. Antunes-Ricardo M, Moreno-García BE, Gutiérrez-Uribe JA, et al. Induction of apoptosis in colon cancer cells treated with isorhamnetin glycosides from Opuntia ficus-indica pads. *Plant Foods Hum Nutr*. 2014;69(4):331–336. doi:10.1007/s11130-014-0438-5
48. Jaramillo S, Lopez S, Varela LM, et al. The flavonol isorhamnetin exhibits cytotoxic effects on human colon cancer cells. *J Agric Food Chem*. 2010;58(20):10869–10875. doi:10.1021/jf102669p
49. Zhao X, Liu Z, Liu H, et al. Hybrid molecules based on caffeic acid as potential therapeutics: a focused review. *Eur J Med Chem*. 2022;243:114745. doi:10.1016/j.ejmech.2022.114745
50. Alam F, Mohammadin K, Shafique Z, et al. Citrus flavonoids as potential therapeutic agents: a review. *Phytother Res*. 2022;36(4):1417–1441. doi:10.1002/ptr.7261
51. Nazzaro-Porro M. Azelaic acid. *J Am Acad Dermatol*. 1987;17(6):1033–1041. doi:10.1016/s0190-9622(87)70294-1
52. Eichenfield DZ, Sprague J, Eichenfield LF. Management of acne vulgaris: a review. *JAMA*. 2021;326(20):2055–2067. doi:10.1001/jama.2021.17633
53. Sitkovsky MV, Lukashev D, Apasov S, et al. Physiological control of immune response and inflammatory tissue damage by hypoxia-inducible factors and adenosine A2A receptors. *Annu Rev Immunol*. 2004;22(1):657–682. doi:10.1146/annurev.immunol.22.012703.104731
54. Alam MS, Kurtz CC, Rowlett RM, et al. CD73 is expressed by human regulatory T helper cells and suppresses proinflammatory cytokine production and Helicobacter felis-induced gastritis in mice. *J Infect Dis*. 2009;199(4):494–504. doi:10.1086/596205
55. Fang JY, Richardson BC. The MAPK signalling pathways and colorectal cancer. *Lancet Oncol*. 2005;6(5):322–327. doi:10.1016/s1470-2045(05)70168-6
56. Chakraborty J, Chakraborty S, Chakraborty S, et al. Entanglement of MAPK pathways with gene expression and its omnipresence in the etiology for cancer and neurodegenerative disorders. *Biochim Biophys Acta Gene Regul Mech*. 2023;1866(4):194988. doi:10.1016/j.bbagrm.2023.194988
57. Davies M, Robinson M, Smith E, et al. Induction of an epithelial to mesenchymal transition in human immortal and malignant keratinocytes by TGF-beta1 involves MAPK, Smad and AP-1 signalling pathways. *J Cell Biochem*. 2005;95(5):918–931. doi:10.1002/jcb.20458
58. Kam AE, Masood A, Shroff RT. Current and emerging therapies for advanced biliary tract cancers. *Lancet Gastroenterol Hepatol*. 2021;6(11):956–969. doi:10.1016/s2468-1253(21)00171-0
59. Chang Y, Tian Y, Zhou D, et al. Gentiopicroside ameliorates ethanol-induced gastritis via regulating MMP-10 and pERK1/2 signaling. *Int Immunopharmacol*. 2021;90:107213. doi:10.1016/j.intimp.2020.107213
60. Jackson CB, Judd LM, Menheniott TR, et al. Augmented gp130-mediated cytokine signalling accompanies human gastric cancer progression. *J Pathol*. 2007;213(2):140–151. doi:10.1002/path.2218
61. Nam HH, Kim JS, Lee J, et al. Pharmacological effects of Agastache rugosa against gastritis using a network pharmacology approach. *Biomolecules*. 2020;10(9):1298. doi:10.3390/biom10091298
62. Yang Y, Lee GJ, Yoon DH, et al. ERK1- and TBK1-targeted anti-inflammatory activity of an ethanol extract of Dryopteris crassirhizoma. *J Ethnopharmacol*. 2013;145(2):499–508. doi:10.1016/j.jep.2012.11.019
63. Zhao Y, Zheng W. Deciphering the antitumoral potential of the bioactive metabolites from medicinal mushroom Inonotus obliquus. *J Ethnopharmacol*. 2021;265:113321. doi:10.1016/j.jep.2020.113321
64. Elhadidy MG, El Nashar EM, Alghamdi MA, et al. A novel gastroprotective effect of zeaxanthin against stress-induced gastritis in male rats targeting the expression of HIF-1α, TFF-1 and MMP-9 through PI3K/Akt/JNK signaling pathway. *Life Sci*. 2021;273:119297. doi:10.1016/j.lfs.2021.119297
65. Mahauad-Fernandez WD, Felsher DW. The myc and ras partnership in cancer: indistinguishable alliance or contextual relationship? *Cancer Res*. 2020;80(18):3799–3802. doi:10.1158/0008-5472.Can-20-0787
66. Dang CV. MYC on the path to cancer. *Cell*. 2012;149(1):22–35. doi:10.1016/j.cell.2012.03.003
67. Han H, Ding G, Wang S, et al. Long non-coding RNA LOC339059 attenuates IL-6/STAT3-signaling-mediated PDL1 expression and macrophage M2 polarization by interacting with c-Myc in gastric cancer. *Cancers*. 2023;15(22):5313. doi:10.3390/cancers15225313

68. Fujimori Y, Inokuchi M, Takagi Y, et al. Prognostic value of RKIP and p-ERK in gastric cancer. *J Exp Clin Cancer Res*. 2012;31(1):30. doi:10.1186/1756-9966-31-30
69. Zuo Z, Liu J, Sun Z, et al. ERK and c-Myc signaling in host-derived tumor endothelial cells is essential for solid tumor growth. *Proc Natl Acad Sci*. 2023;120(1):e2211927120. doi:10.1073/pnas.2211927120

Drug Design, Development and Therapy Dovepress

Publish your work in this journal

Drug Design, Development and Therapy is an international, peer-reviewed open-access journal that spans the spectrum of drug design and development through to clinical applications. Clinical outcomes, patient safety, and programs for the development and effective, safe, and sustained use of medicines are a feature of the journal, which has also been accepted for indexing on PubMed Central. The manuscript management system is completely online and includes a very quick and fair peer-review system, which is all easy to use. Visit http://www.dovepress.com/testimonials.php to read real quotes from published authors.

Submit your manuscript here: https://www.dovepress.com/drug-design-development-and-therapy-journal